Geochemistry, Geophysics, Geosystems®

RESEARCH ARTICLE
10.1029/2025GC012585

Silicate and Carbonate Weathering Perturbation at the Eocene-Oligocene Transition Recorded by Mg Isotopes

Adam D. Sproson[1,2,3], Toshihiro Yoshimura[1], Shigeyuki Wakaki[4,5], Takahiro Aze[2], Yusuke Yokoyama[1,2], Tsuyoshi Ishikawa[4], and Naohiko Ohkouchi[1]

[1]Biogeochemistry Research Center, Japan Agency for Marine-Earth Science and Technology, Yokosuka, Japan, [2]Atmosphere and Ocean Research Institute, The University of Tokyo, Kashiwa, Japan, [3]National Oceanography Centre, Southampton, UK, [4]Kochi Institute for Core Sample Research, Japan Agency for Marine-Earth Science and Technology, Nankoku, Japan, [5]National Museum of Japanese History, Sakura, Japan

Key Points:

- Mg isotopes in the carbonate, reactive, and residual fraction of sediments resolve unique weathering signatures on sub-Myr timescales
- Mg isotope variation reveals that Antarctic ice sheet growth increased Antarctic bedrock silicate and shelf carbonate weathering
- Silicate and carbonate weathering contributed to atmospheric CO_2 drawdown and a deepening of the carbonate compensation, respectively

Supporting Information:

Supporting Information may be found in the online version of this article.

Correspondence to:

A. D. Sproson,
adam.sproson@noc.ac.uk

Citation:

Sproson, A. D., Yoshimura, T., Wakaki, S., Aze, T., Yokoyama, Y., Ishikawa, T., & Ohkouchi, N. (2026). Silicate and carbonate weathering perturbation at the Eocene-Oligocene transition recorded by Mg isotopes. *Geochemistry, Geophysics, Geosystems*, *27*, e2025GC012585. https://doi.org/10.1029/2025GC012585

Received 28 JUL 2025
Accepted 9 JAN 2026

Author Contributions:

Conceptualization: Adam D. Sproson, Toshihiro Yoshimura
Data curation: Adam D. Sproson
Formal analysis: Adam D. Sproson
Funding acquisition: Adam D. Sproson, Toshihiro Yoshimura, Shigeyuki Wakaki
Investigation: Adam D. Sproson, Toshihiro Yoshimura, Takahiro Aze
Methodology: Adam D. Sproson, Toshihiro Yoshimura, Shigeyuki Wakaki, Takahiro Aze
Project administration: Adam D. Sproson, Toshihiro Yoshimura,

Abstract During the Eocene-Oligocene Transition (ca. 34 Ma), the Earth underwent a dramatic decline in atmospheric CO_2, global cooling, a deepening of the carbonate compensation depth (CCD), and the formation of a permanent ice sheet on Antarctica. The expansion of Antarctic glaciers eroded the underlying bedrock and increased the weathering flux to the ocean. However, the role silicate and carbonate weathering play in atmospheric CO_2 removal and the CCD through Ca^{2+} and alkalinity production is poorly understood. Magnesium isotopes ($\delta^{26}Mg$) are fractionated during carbonate and clay mineral formation and can be used to quantify the relative flux from silicate and carbonate weathering. Here, we report the $\delta^{26}Mg$ composition of the carbonate, reactive (ferromanganese coatings), and residual (silicate) fraction of marine sediments from the Kerguelen Plateau (Ocean Drilling Program Site 738), near a major drainage system of the East Antarctic Ice Sheet, to explore the response of subglacial and shelf weathering to ice sheet expansion. The $\delta^{26}Mg$ of the carbonate fraction (−2.29‰ to −0.95‰), reactive fraction (−0.36‰ to 0.10‰), and residual fraction (−0.05‰ to 0.55‰) display similar values to surface-dwelling calcareous nannofossils, deep-water ferromanganese nodules, and Antarctic bedrock, respectively. Isotope fluctuations in all three phases suggest that the formation of the Antarctic ice sheet drove efficient chemical weathering of underlying silicate bedrock, which was rapidly transported to the Southern Ocean, resulting in further CO_2 drawdown, while a local sea-level low stand exposed carbonates on the Antarctic continental shelf to weathering, contributing to a deepening of the CCD.

Plain Language Summary A permanent ice sheet formed on Antarctica 34 million years ago owing to a drop in atmospheric carbon dioxide concentration and global temperatures. As the ice sheet grew, it eroded rocks in its path, transporting the resulting material to the ocean and lowered the global sea level, exposing the continental shelf to the atmosphere. We analyzed the chemistry of sediments deposited near Antarctica, which provides a record of past environmental change, to understand how these two processes affected the global climate. Our study found that silicate rocks were eroded from the Antarctic continent, which converted carbon dioxide to alkalinity leading to further cooling. The exposure of carbonates on the continental shelf delivered calcium to the ocean, contributing to calcite precipitation at greater depths in the deep sea. This study helps disentangle competing hypotheses that explain the carbon cycle perturbation found at the tipping point between a greenhouse and icehouse world and suggests that similar chemical analysis from carefully selected locations could unlock important information pertaining to regional climate reorganizations in the geological past.

1. Introduction

The Eocene-Oligocene Transition (EOT) is a period of approximately 790 kyr (34.2–33.5 Ma) that demarcates the shift from Eocene greenhouse conditions to Oligocene icehouse conditions (Gradstein, 2012; Hutchinson et al., 2021). The EOT is defined by a dramatic two-step increase in the benthic foraminiferal oxygen isotope ($\delta^{18}O$) record, which represents a global cooling of ∼2.5°C and the formation of a permanent, large-scale Antarctic ice sheet (Bohaty et al., 2012; Coxall et al., 2005; Lear et al., 2008; Zachos et al., 2001). The two principal triggers put forth to explain this transition are a decline in atmospheric CO_2 (DeConto & Pollard, 2003; DeConto et al., 2008; Hutchinson et al., 2021) and the opening of the Drake Passage and Tasman Gateway (Kennett, 1977). The former is supported by atmospheric CO_2 reconstructions which suggest a decrease of 600 to 300 ppmv across the EOT (Anagnostou et al., 2016; Pagani et al., 2011; Pearson et al., 2009; Zhang et al., 2013), while the latter lacks support from the timing of gateway opening (Hill et al., 2013; Scher et al., 2015).

Shigeyuki Wakaki, Yusuke Yokoyama, Tsuyoshi Ishikawa, Naohiko Ohkouchi
Resources: Adam D. Sproson, Toshihiro Yoshimura, Yusuke Yokoyama, Tsuyoshi Ishikawa, Naohiko Ohkouchi
Supervision: Toshihiro Yoshimura, Shigeyuki Wakaki, Yusuke Yokoyama, Tsuyoshi Ishikawa, Naohiko Ohkouchi
Validation: Adam D. Sproson, Toshihiro Yoshimura, Takahiro Aze
Visualization: Adam D. Sproson
Writing – original draft: Adam D. Sproson
Writing – review & editing: Adam D. Sproson, Toshihiro Yoshimura, Shigeyuki Wakaki, Takahiro Aze, Yusuke Yokoyama, Tsuyoshi Ishikawa, Naohiko Ohkouchi

The emergence of an ice sheet on Antarctica generated a surge in glacial erosion, facilitating greater chemical weatherability of Antarctic bedrock. Increased Antarctic silicate weathering has been invoked as a source of alkalinity to the ocean, removing CO_2 from the atmosphere and providing a positive feedback on glaciation (Basak & Martin, 2013; Ravizza & Peucker-Ehrenbrink, 2003; Scher et al., 2011; Zachos & Kump, 2005). This assumes that alkalinity is efficiently transported from Antarctica to the ocean without forming secondary silicates (e.g., clay), which would convert alkalinity back to CO_2 (e.g., Pogge von Strandmann & Henderson, 2015). Silicate weathering could also have supplied calcium ions to the ocean and raised the ocean calcite saturation state (Ω) leading to an observed deepening of the carbonate compensation depth (CCD) at the EOT (Lyle et al., 2008; Rea & Lyle, 2005). Alternatively, greater weatherability of glacially eroded Antarctic carbonates or shelf carbonates, exposed during a fall in sea-level, may be responsible for the CCD deepening (Armstrong McKay et al., 2016; Basak & Martin, 2013; Coxall et al., 2005; Griffith et al., 2011; Lear & Rosenthal, 2006; Merico et al., 2008; Zachos et al., 1999). These competing hypotheses have been investigated using radiogenic isotopes, proxies for Antarctic weathering provenance (Basak & Martin, 2013; Ravizza & Peucker-Ehrenbrink, 2003; Scher et al., 2011), and stable calcium isotopes, related to changes in ocean Ca inputs/outputs (Griffith et al., 2011). However, these systems struggle to determine (a) the role clay formation plays in mitigating silicate weathering's influence on global climate and (b) the source of Ca^{2+} in the ocean.

Magnesium isotopes are fractionated during mineral formation, whereby carbonates (e.g., calcite and dolomite) become depleted relative to the precipitating fluid (by ~1‰–4‰) and Mg-clays become enriched in ^{26}Mg (Galy et al., 2002; Higgins & Schrag, 2010; Pogge von Strandmann, 2008; Teng, Li, Rudnick, & Gardner, 2010; Tipper et al., 2006; Tipper et al., 2012). With Mg-carbonates and Mg-clays representing two of the major sources and sinks of Mg to the ocean, seawater $\delta^{26}Mg$ records can be used to quantify the relative contribution of carbonate and silicate fluxes to the ocean and help elucidate carbon cycle dynamics during Earth's geological past (Gothmann et al., 2017; Higgins & Schrag, 2015; Pogge von Strandmann et al., 2014). The $\delta^{26}Mg$ values of foraminifera, bulk limestones, corals, dolomites, and evaporites provide an archive for the Mg isotope composition of seawater that has been used to trace changes in silicate and carbonate weathering and Mg uptake into dolomites and marine clays, but care must be taken to assess the impacts of diagenesis (Gothmann et al., 2017; Higgins & Schrag, 2015; Pogge von Strandmann et al., 2014; Shalev, Bontognali, & Vance, 2021; Shalev, Lazar, et al., 2021). Evidence suggests that ferromanganese nodules and the ferromanganese coatings of sediments could provide an additional archive of seawater $\delta^{26}Mg$ if diagenetic mineral transformation is absent (Fu, 2020; Rose-Koga & Albarède, 2010), but have yet to be utilized for paleoclimate reconstructions.

Due to the limited fractionation of Mg isotopes during magmatic processes, the upper continental crust consists of rocks with a relatively narrow range of $\delta^{26}Mg$ values (−0.3‰ to −0.1‰; Huang et al., 2016; Teng, Li, Ke, et al., 2010; Teng et al., 2016). However, during chemical weathering, Mg isotopes become fractionated by up to 2‰ with the preferential retention of the heavier Mg in weathering residues, which become progressively enriched in ^{26}Mg as weathering intensifies (Huang et al., 2012; Liu et al., 2014; Teng, Li, Rudnick, & Gardner, 2010; Wimpenny et al., 2014). This has been observed in residues from basaltic terrains which display a $\delta^{26}Mg$ increase from unaltered bedrock to weathered saprolites (Huang et al., 2012; Liu et al., 2014; Teng, Li, Rudnick, & Gardner, 2010). The Mg isotope analysis of fine-grained siliciclastic material can therefore be used to reconstruct relative changes in chemical weathering intensity during major geological events (Huang et al., 2016).

Here, we measure $\delta^{26}Mg$ in marine sediment phases to overcome limitations in radiogenic and other stable isotope studies and (a) ascertain the role of clay formation in mitigating CO_2 drawdown through Antarctic silicate weathering and (b) the source of Antarctic calcium ions to CCD deepening at the EOT. Samples were selected from Ocean Drilling Program Site 738 on the Kerguelen Plateau because it has been shown to record water mass and weathering signals derived from the nearby East Antarctic during the Paleogene with remarkable fidelity (Basak & Martin, 2013; Scher et al., 2011, 2014). We utilized a sequential leaching method developed previously for radiogenic isotopes (Basak et al., 2011; Wilson et al., 2013) to separate the carbonate and associated Mn and Fe oxides, reactive (ferromanganese coatings), and residual (e.g., silicates) fractions from Site 738 sediments to investigate their potential to record the $\delta^{26}Mg$ of pristine calcareous nannofossils inhabiting Antarctic Surface Water (Ehrmann & Mackensen, 1992), Antarctic bottom waters (Scher et al., 2011), and East Antarctic bedrock (Basak & Martin, 2013), respectively. The isolated fractions were also analyzed for rare-earth element and yttrium (REY) and major and trace element concentrations to help interpret isotope results and assess the level of phase contamination and diagenesis. We show that sequential leaching provides relatively pristine environmental signals. Observed $\delta^{26}Mg$ perturbations at the EOT support a regime shift to more efficient silicate weathering and

aerial exposure of shelf carbonates, which helped drive climate-weathering feedback and a deepening of the CCD, respectively.

2. Materials and Methods

2.1. Study Location, Core Sampling and Age Model

ODP Site 738 is located on the Southern Kerguelen Plateau (62.7°S, 82.8°E) and is currently bathed in Circumpolar Deep Water at a water depth of 2,252 m (see Scher et al., 2011). The Kerguelen Plateau causes the Southern Antarctic Circumpolar Current Front to deflect northward where it intensifies and deepens to form the Kerguelen deep western boundary current, bringing cold deep water and suspended sediment from the Antarctic margin to Site 738 (Fukamachi et al., 2010; Speer & Forbes, 1994). Sources of bottom water in the Kerguelen deep western boundary current include nearby Prydz Bay, Wilkes Land, the Adélie coast, and the Ross Sea on the Antarctic continental shelf (Orsi et al., 1999). The proximity to East Antarctic terrestrial material combined with the subsequent transport of suspended sediment by the Kerguelen deep western boundary current makes the Southern Kerguelen Plateau a unique location for studying weathering and erosion products from Antarctica during the Cenozoic (Basak & Martin, 2013; Scher et al., 2011).

Site 738 sediment largely consists of biogenic calcareous nannofossils (>90%) with the remainder composed of opal and terrigenous sediment (Ehrmann & Mackensen, 1992). Samples were selected following previous studies (Basak & Martin, 2013) at an average interval of 20 cm between ∼18.2 and 27.2 m below the sea floor. A previously determined age model based on biostratigraphic datums and oxygen and carbon ($\delta^{13}C$) isotope stratigraphy (Bohaty et al., 2012) constrains the studied interval to ∼33.42 to 34.22 Ma. This covers key $\delta^{18}O$ and chronostratigraphic characteristics of EOT deep-sea marine records (Hutchinson et al., 2021) such as: the first step increase in $\delta^{18}O$ (aka "Step 1"); the Eocene Oligocene Boundary (EOB); the rapid $\delta^{18}O$ increase of >0.7‰ known as the Earliest Oligocene oxygen isotope step (EOIS); the EOT; and the Early Oligocene glacial maximum (EOGM).

2.2. Sequential Leaching of Sediments

Samples were dried, crushed, and homogenized using an agate mortar and pestle before undergoing leaching techniques to extract the carbonate and Mn-Fe-oxides, reactive, and residual (bulk and fine) fractions from sediments, developed previously for radiogenic isotope analysis (Basak et al., 2011; Tessier et al., 1979; Wilson et al., 2013). To test the impact of the carbonate fraction on the capability of ferromanganese coatings to reconstruct the $\delta^{26}Mg$ composition of seawater, roughly 0.5 g of sediment was treated using 5 mL of 0.02 M hydroxylamine hydrochloride in 10% acetic acid for 1.5 hr (Wilson et al., 2013). The sample was centrifuged, and the remaining supernatant was extracted, dried, and redissolved in 1 M HNO_3 (TAMAPURE, Tama Chemical Corp., Kanagawa, Japan). This solution represents the carbonates and Mn-Fe-oxides (hereafter the "carbonate" fraction) in sediments (Wilson et al., 2013).

The remaining sample was decarbonated using 10 mL of 1 M Na acetate buffered acetic acid (2.7%) at a pH of 5 (Basak et al., 2011). This step was repeated as necessary to ensure complete carbonate removal. The decarbonated sample was then treated with 5 mL of 1 M hydroxylamine hydrochloride in 25% acetic acid for ∼24 hr to ensure complete removal of any remaining ferromanganese coatings (Basak et al., 2011; Basak & Martin, 2013). The remaining residue was rinsed three times with distilled (Milli-Q™) water and dried. Approximately 0.05 g of dried residue was dissolved in 21 M HF and 14 M HNO_3 (3 mL: 1 mL) for several days at 40°C and repeated as necessary (Basak et al., 2011). The remaining solution was dried down and redissolved in 6 M HCl for ∼24 hr to convert any fluorides to chlorides and then dried down and redissolved in 1 M HNO_3. This solution represents the bulk detrital silicates (hereafter the "residual" fraction) in sediments (Basak & Martin, 2013; Tessier et al., 1979; Basak et al., 2011; Wilson et al., 2013).

A fresh ∼0.5 g of sample was decarbonated using several additions of 10 mL of 1 M Na acetate buffered acetic acid (2.7%) at a pH of 5. The remaining residue was rinsed three times with distilled water before treating with 5 mL of 0.02 M hydroxylamine hydrochloride in 25% acetic acid on a rotary shaker for 1.5 h (Basak et al., 2011). After centrifugation, the remaining supernatant was dried down and redissolved in 1 M HNO_3. This solution represents the ferromanganese coatings (hereafter the "reactive" fraction) on sediments (Basak & Martin, 2013; Basak et al., 2011; Tessier et al., 1979; Wilson et al., 2013). The samples were then treated with 5 mL of 1 M

hydroxylamine hydrochloride in 25% acetic acid for ~24 hr. The remaining residue was rinsed three times with distilled water and dried. To remove grain size effects, the dried residue was sieved (<63 μm) and dissolved as previously mentioned. This solution represents the fine detrital silicates (hereafter the "fine" fraction) in sediments. All sample solutions were split into two aliquots for element and isotope analysis.

2.3. Elemental Concentrations

Major, trace, and rare-earth element concentrations were measured using a quadrupole ICP-MS (iCap Q, Thermo Fisher Scientific, Bremen, Germany) at the Biogeochemistry Research Center, Japan Agency for Marine-Earth Science and Technology (JAMSTEC). To correct for instrument drift, internal standards of Be-Sc-Y-In and Be-In-Re were used for major and trace elements and REY, respectively. Oxide interference on the rare-earth elements was corrected using a range of Pr, Nd, Gd, Ce, Ba, Eu, Gd, and Tb standards. Signal intensities were converted to concentrations using a calibration based on ICP Multi-element Standards IV (Merck KGaA, Darmstadt, Germany), Metals Standard Solution VII (Kanto Chemical, Tokyo, Japan), and XSTC-VII and XSTC-1957 standards (SPEX CertiPrep, Metuchen, USA). Elemental data are presented as mass of element in leachate/bulk mass of sediment leached.

2.4. Mg Purification and Isotope Measurement

Magnesium in the carbonate, reactive, residual, and fine solutions were separated from the sample matrix by ion chromatography using a 930 Compact Ion Chromatography Flex System (Metrohm AG, Herisau, Switzerland) coupled to an Agilent 1260 Infinity II Bio-Inert analytical-scale Fraction Collector system (Agilent Technologies, Santa Clara) at the Biogeochemistry Research Center, JAMSTEC (Yoshimura et al., 2018). Sample solutions were dried down and redissolved in 8 mM HNO_3 (TAMAPURE AA-100, Tama Chemical Corp., Kanagawa, Japan) and eluted through a Metrohm Metrosep C6-250/4.0 column containing silica gel with functionalized carboxyl groups at a flow rate of 0.9 mL min^{-1} (Araoka & Yoshimura, 2019). All other settings are reported elsewhere (Yoshimura et al., 2018). A time-triggered mode provided continuous collections of baseline-separated Mg peaks, which were pooled in 7-ml PFA vials (Savillex, Minnesota) and then dried down ready for isotope analysis.

The isotopic composition of the purified Mg solutions was determined by a Multi-Collector Inductively Coupled Plasma Mass Spectrometer (Neptune, Thermo Fisher Scientific, Bremen, Germany) at the Kochi Institute for Core Sample Research, JAMSTEC (Eom et al., 2022). Samples and reference reagents were prepared as ~100 ng Mg solutions using 0.1 M HCl. This yielded a 5 V ^{24}Mg ion beam, which, along with ^{25}Mg and ^{26}Mg ion beams, was simultaneously measured by Faraday cup detectors with 1,011 Ω resistor amps. Measurements were performed using sample–standard (DSM-3) bracketing for 40 cycles of 4 s. The isotope ratios were reported as follows: $\delta^{26}Mg = [(^{26}Mg/^{24}Mg)_{sample}/(^{26}Mg/^{24}Mg)_{DSM-3} - 1] \times 1{,}000$. Long-term reproducibility of $\delta^{26}Mg$ (2SE = 0.11‰) and $\delta^{25}Mg$ (2SE = 0.07‰) was determined using multiple measurements of Cambridge-1, which has a respective value of −2.61‰ and −1.34‰ ($n = 13$) consistent with previous studies (Teng, 2017).

3. Results

3.1. Element Ratios

The respective Li/Ca and Mg/Ca ratios of the carbonate fraction range from 4.6 to 33.1 μmol/mol and 4.5 to 11.3 mmol/mol ($n = 32$), consistent with low-Mg carbonates and/or aragonite (Murphy et al., 2022). A Sr/Ca value of 1.3 ± 0.2 mmol/mol ($n = 32$) is lower than typical values for aragonite of ~10 mmol/mol (Kinsman, 1969; Lowenstam, 1961) but comparable to other carbonate-rich nannofossil oozes (Ando et al., 2006). The carbonate fractions Al/Ca, Fe/Ca, and Li/Na are generally low but highly variable, ranging from 0.3 to 1,024.8, 40.6 to 422.8, and 125.1 to 399.0 μmol/mol ($n = 32$), respectively. Sample 3H-4W 113–114 lies outside the interquartile range for Al/Ca and Fe/Ca and after removal the respective ranges become 88.5–1,024.8 and 40.6–137.6 μmol/mol ($n = 31$). The Rb/Sr ratios of the carbonate fraction range from 4.4 to 7.8 mmol/mol. The Li/Ca, Mg/Ca, Al/Ca, Fe/Ca, and Li/Na ratios are relatively low at ~6 μmol/mol, ~5 mmol/mol, ~120 μmol/mol, ~55 μmol/mol, and ~165 μmol/mol during the latest Eocene, increasing after 33.75 Ma to maximum values at ~33.70 Ma between the EOB and the EOIS, before decreasing to pre-excursion values during the EOBM (Figures 1b–1e and 1i). The Mn/Sr ratios are highly variable, increasing from 34.00 to 33.88 Ma, 33.83 to

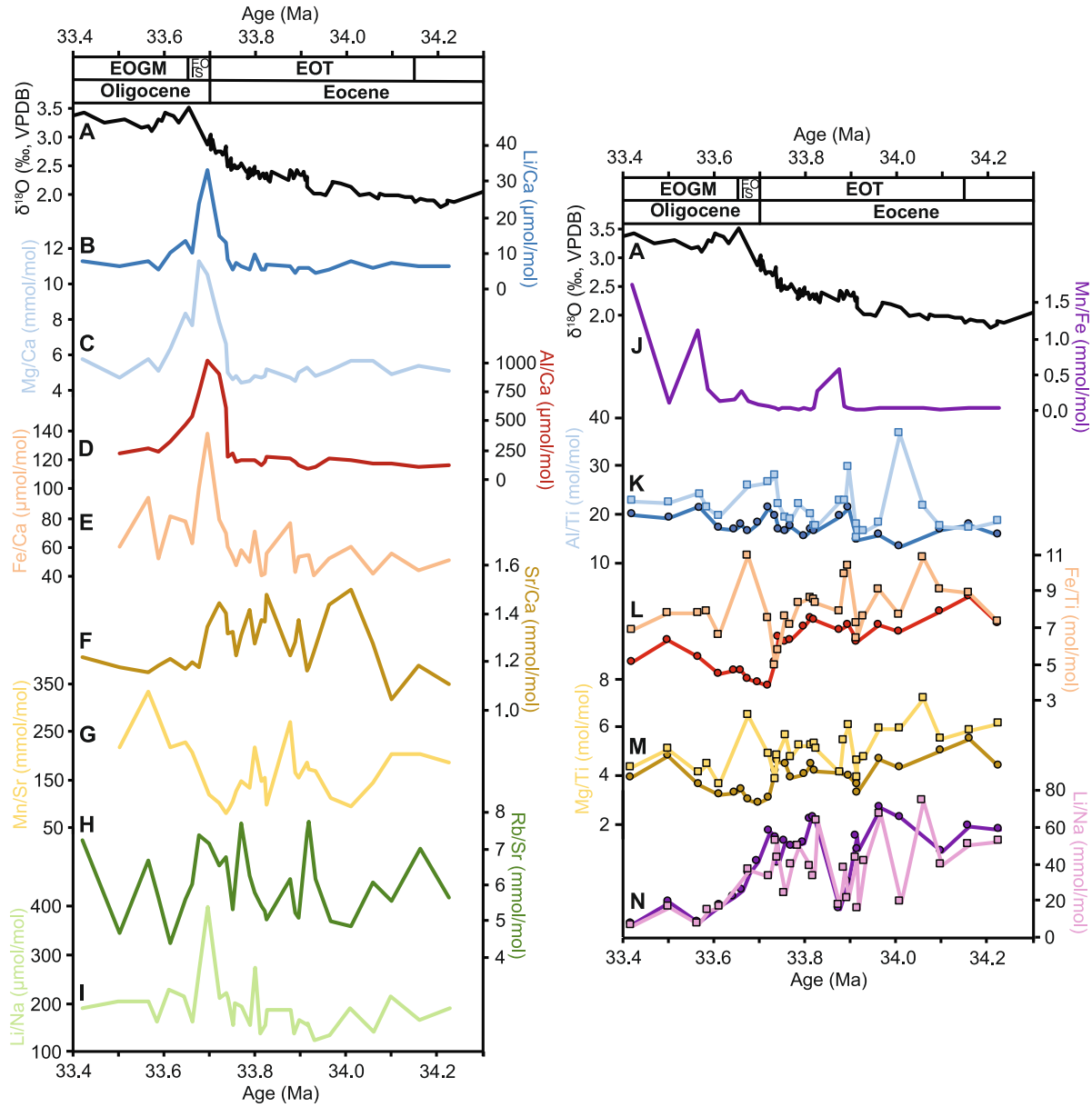

Figure 1. Element ratios for the carbonate (b–i), reactive (j), and residual (circles) and fine (squares) (k–n) fractions. Sample 3H-4W 113–114 has not been included for Al/Ca and Fe/Ca (see text for details). The Site 738 oxygen isotope record is presented in a (Scher et al., 2011).

33.80 Ma, and 33.74 to 33.57 Ma by 118–251 mmol/mol (Figure 1g). The Sr/Ca and Rb/Sr ratios are relatively invariable close to the long-term average (Figures 1f and 1h).

The Mn/Fe ratios of the reactive fraction range from 17.6 to 1,758.0 mmol/mol ($n = 32$), which is generally lower than ferromanganese nodules (Mn/Fe = 1–5 mol/mol) and reactive leaches (Mn/Fe = 0.74–3.70 mol/mol) previously recorded (Axelsson et al., 2002; Basak et al., 2011; Menendez et al., 2019). The reactive Mn/Fe ratios are relatively low (0.04 mmol/mol) before 33.74 Ma and then increase towards the EOBM with several peaks observed at 33.88, 33.57, and 33.42 Ma (Figure 1j). The residual fraction has an Al/Ti, Fe/Ti, Mg/Ti, and Li/Na range of 13.3–21.5 mol/mol, 3.8–8.7 mol/mol, 2.8–5.5 mol/mol, and 6.5–70.9 mmol/mol ($n = 26$), respectively. Residual fractions Al/Ti, Fe/Ti, Mg/Ti, and Li/Na are within the uncertainty of the fine fraction, which records ranges of 15.1–36.4 mol/mol, 4.9–11.0 mol/mol, 3.6–7.2 mol/mol, and 5.5–74.0 mmol/mol ($n = 27$), respectively. The Al/Ti, Fe/Ti, Mg/Ti, and Li/Na of the residual and fine fraction display similar first-order trends, while the fine fraction records more higher-order variability (Figures 1k–1n).

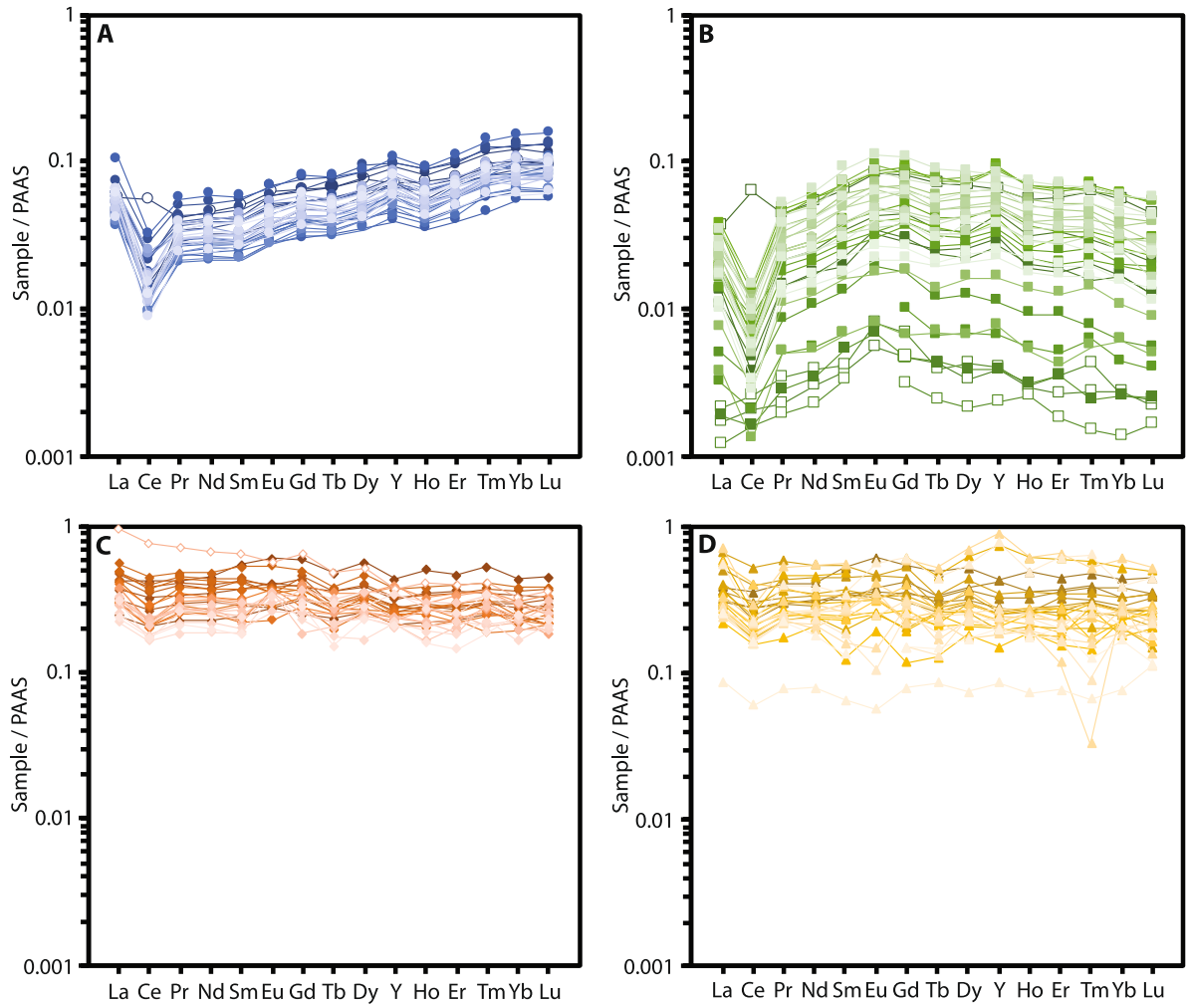

Figure 2. Rare-earth element and yttrium (REY) patterns for the carbonate (a), reactive (b), residual (c), and fine (d) fractions. REY patterns are normalized to values for the Post-Archean Australian Shale (Taylor & McLennan, 1985). Open symbols represent samples that do not fit the expected REY pattern (see Section 3.2 for details).

3.2. REY Patterns

The REY patterns normalized to Post-Archean Australian Shale (PAAS; Taylor & McLennan, 1985) are indistinguishable from observations from Pb and Nd isotope studies that used a similar leaching method to separate the carbonate, reactive, and residual fraction from marine sediments (Basak et al., 2011; Basak & Martin, 2013; Martin et al., 2010; Wilson et al., 2013). The negative Ce anomaly, LREE enrichment, and high Y/Ho observed in the carbonate fraction REY patterns (Figure 2a) are identical to acetic acid leaching of the Mn oxide and carbonate phase from marine sediments (Martin et al., 2010; Wilson et al., 2013). The reactive fraction REY patterns (Figure 2b) record the typical Ce anomalies and MREE bulge observed in reduced pore waters, marine sediments, and Site 738 fish teeth, indicative of an Fe oxide source (Basak et al., 2011; Bayon et al., 2002; Haley et al., 2004; Kim et al., 2012; Martin et al., 2010; Scher et al., 2011; Wilson et al., 2013).

The residual (Figure 2c) and fine (Figure 2d) fractions display a similar REY pattern, which is relatively flat, indicating a similar composition to PAAS and therefore a recycled or weathered terrestrial component of the upper continental crust (Martin et al., 2010; Wilson et al., 2013). Some detrital samples record a slight Ce anomaly indicating the presence of Fe oxides (Martin et al., 2010) despite the use of a strong reductive leaching step (Gutjahr et al., 2007). Several samples do not fit these general trends and need to be treated with caution when interpreting isotope results (open symbols in Figure 2). The carbonate and reactive fraction of sample 3H-4W 17–18 has a positive Ce anomaly, the reactive fraction of sample 3H-4W 113–114, 3H-4W 99.5–100.5, and 3H-4W

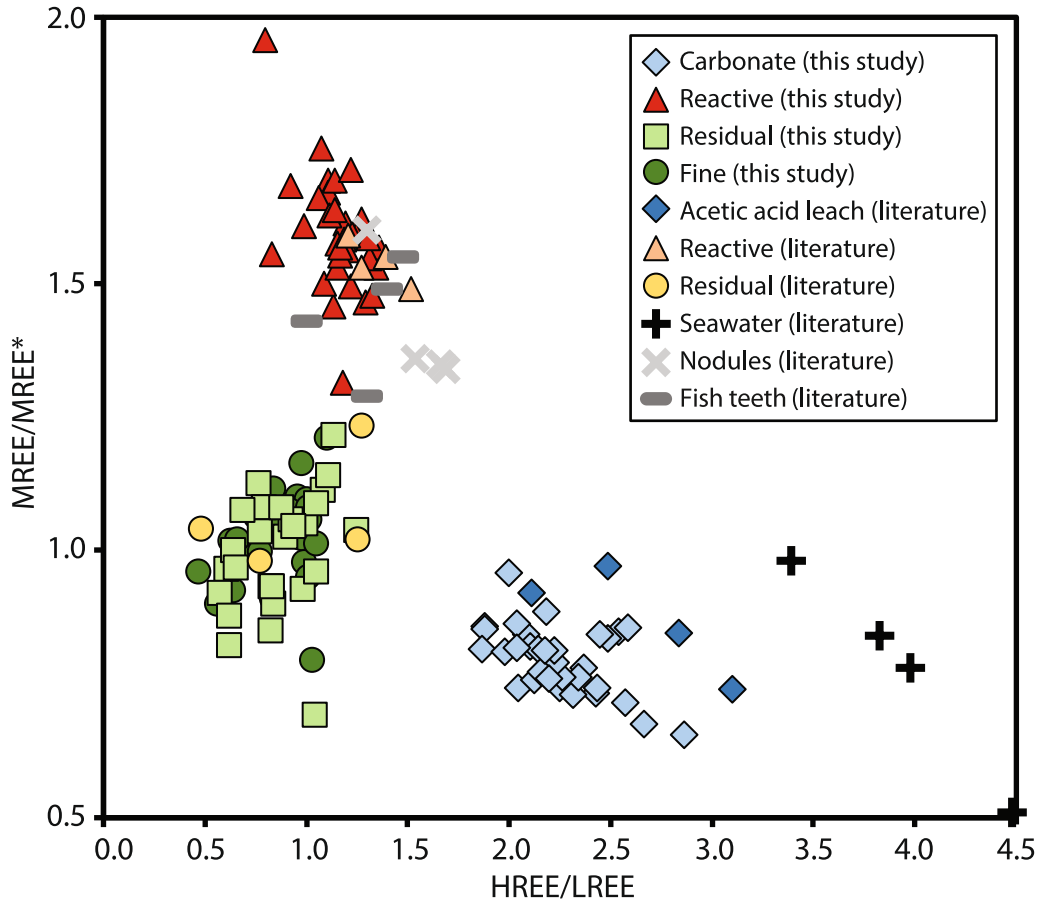

Figure 3. A comparison of Post-Archean Australian Shale normalized HREE/LREE (Tm + Yb + Lu)/(La + Pr + Nd) versus MREE/MREE* (Gd + Tb + Dy/average of HREE and LREE) for the carbonate (light blue diamonds), reactive (red triangles), residual (light green squares), and fine (dark green circles) fraction with acetic acid leaches (dark blue diamonds; Martin et al., 2010), reactive fraction (light orange triangles; Martin et al., 2010), residual fraction (yellow circles; Martin et al., 2010), seawater (black crosses; Lacan & Jeandel, 2005; Piepgras & Jacobsen, 1992; Zhang et al., 2008), Fe-Mn nodules and particles (gray cross; Jauhari & Pattan, 2017; Sherrell et al., 1999), and fish teeth (gray dash; Martin et al., 2010).

122.5–123.5 lack the negative Ce anomaly and the residual fraction of sample 4H-1W 43.5–44.5 is enriched in the lighter REEs.

The PAAS normalized REEs are separated into HREE (Tm + Tb + Lu), MREE (Gd + Ty + Db), LREE (La + Pr + Nd), and MREE* ([Tm + Yb + Lu + La + Pr + Nd]/2) to facilitate comparison between the sedimentary fractions extracted here and previous studies (Haley et al., 2004; Martin et al., 2010). The respective HREE/LREE ratios for the carbonate, reactive, and residual/fine fraction is 2.25 ± 0.49 (n = 32), 1.16 ± 0.27 (n = 32), and 0.86 ± 0.35 (n = 53), comparable to the acetic acid (2.63 ± 0.86), hydroxylamine hydrochloride (1.35 ± 0.27), and residue (0.94 ± 0.77) fractions of Cenozoic and Cretaceous marine sediments (Figure 3). The MREE/MREE* ratios quantify the extent of the MREE bulge, which is more pronounced in the reactive phase of sediments reported here (1.59 ± 0.22) and previously (1.54 ± 0.08) when compared to the carbonate (0.80 ± 0.13) and residual/fine (1.03 ± 0.20) fraction (Figure 3). The HREE/LREE versus MREE/MREE* relationship for the carbonate fraction is similar to Pacific, North Atlantic, and Indian Ocean seawater although generally less enriched in the HREEs (Figure 3; De Baar et al., 1985; Lacan & Jeandel, 2005; Piepgras & Jacobsen, 1992; Zhang et al., 2008). The reactive and residual/fine fraction, respectively, resemble Fe-Mn nodules and fish teeth (Axelsson et al., 2002; Jauhari & Pattan, 2017; Martin et al., 2010; Sherrell et al., 1999) and residual silicates (Bayon et al., 2002; Gutjahr et al., 2007; Martin et al., 2010), indicating a different source of REEs.

3.3. Mg Isotopes

The $\delta^{26}Mg$ of the carbonate ($\delta^{26}Mg_{carbonate}$), reactive ($\delta^{26}Mg_{reactive}$), residual ($\delta^{26}Mg_{residual}$), and fine ($\delta^{26}Mg_{fine}$) fraction is $-1.67‰ \pm 0.66‰$ ($n = 32$), $-0.10‰ \pm 0.25‰$ ($n = 32$), $0.17‰ \pm 0.71‰$ ($n = 26$), and $0.14‰ \pm 0.26‰$ ($n = 27$), respectively (Table S4). Residual fraction sample 3H-6W 113–114 has a $\delta^{26}Mg$ value of $-1.65‰ \pm 0.02‰$, like the carbonate fraction and outside the interquartile range. After removal the average $\delta^{26}Mg_{reactive}$ increases to $0.23‰ \pm 0.09‰$, within the uncertainty of the fine fraction. The $\delta^{26}Mg_{carbonate}$ values are consistent with Late Eocene-Early Oligocene aragonite corals, which record a Mg isotope value of $-1.95‰$ to $-1.64‰$ (Gothmann et al., 2017), but is substantially higher than the <63 ($\delta^{26}Mg = -4.86‰$ to $-4.40‰$) and 250–450 ($\delta^{26}Mg = -4.91$ to $-4.60‰$) size fractions of pelagic carbonates of a similar age (Higgins & Schrag, 2015). The $\delta^{26}Mg_{carbonate}$ values display an increasing trend towards the EOB (~33.70 Ma) before decreasing to initial values by ~33.50 Ma (Figure 4). Short-term excursions of 0.75–0.90‰ occur between 34.06 and 34.01 Ma, 33.89 and 33.83 Ma, and 33.75 and 33.7 Ma. Carbonate fraction Mg isotopes are weakly correlated to Li/Ca, Mg/Ca, Al/Ca, Fe/Ca, and Li/Na but show no significant relationship with Sr/Ca, Rb/Sr, and Mn/Sr (Figures S1a–S1h in Supporting Information S1), HREE/LREE, and MREE/MREE*.

The $\delta^{26}Mg$ of the reactive fraction lies at the upper end of values reported for Atlantic and Pacific Fe-Mn nodules ($\delta^{26}Mg = -0.01$ to $-2.13‰$) and is indistinguishable from a Fe-Mn nodule ($\delta^{26}Mg = -0.17‰ \pm 0.16‰$) collected from offshore West Antarctica at a depth of 3,475 m (Rose-Koga & Albarède, 2010). The $\delta^{26}Mg_{reactive}$ values fluctuate between 0.10‰ and $-0.24‰$ before ~33.80 Ma and then decrease to $-0.36‰$ by 33.61 Ma (Figure 5), displaying a weak negative correlation with Mn/Fe (Figure S1i in Supporting Information S1) and MREE/MREE* ($R^2 = 0.27$, $p = <0.05$). The residual and fine fraction is isotopically heavier than average crustal values of $-0.22‰$, consistent with weathered silicates which have recorded values of up to 1.80‰ (W.-Y. Li et al., 2010; Liu et al., 2014). The $\delta^{26}Mg_{residual}$ values increase by 0.12‰–0.35‰ from 34.10 to 33.96 Ma and 33.88 to 33.68 Ma before decreasing by 0.24‰–0.30‰ between 33.96 and 33.88 Ma and 33.68 and 33.42 Ma (Figure 4). The fine fraction shows similar long-term variability but differs in the absolute timing of change with several spikes to high values at 33.96, 33.74, and 33.61 Ma (Figure 4). Magnesium isotopes in the reactive and fine fractions show no significant relationship with Al/Ti, Fe/Ti, Mg/Ti, and Li/Na (Figure S2 in Supporting Information S1). The $\delta^{26}Mg$ values of samples with anomalous REY trends (open symbols in Figure 2) display no systematic offsets.

4. Discussion

The $\delta^{26}Mg$ of the carbonate, reactive, residual, and fine fraction extracted from Site 738 sediments could be recording changes in a range of processes that include carbonate mineralogy, diagenesis, contamination from other phases, past seawater chemistry, and/or weathering intensity/provenance. In Sections 4.1 to 4.3, we evaluate the influence of these processes on $\delta^{26}Mg$ values using element ratios, REY patterns, and data from the literature to evaluate their paleoclimate archive potential before discussing the implications for global climate feedback (Section 4.4).

4.1. Evaluation of the Carbonate Fraction as an Archive for the $\delta^{26}Mg$ of Seawater

Carbonate minerals such as foraminifera, limestone, corals, dolomites, and evaporites have been shown to be effective archives for $\delta^{26}Mg_{seawater}$ (e.g., Tipper, 2022). In this section, we assess the carbonate phase of marine sediments as a potential archive for seawater $\delta^{26}Mg$ after considering modifications from diagenesis and sediment dissolution.

4.1.1. Carbonate Mineralogy and Diagenetic Alteration

Site 738 sediments consist of biogenic calcareous nannofossils with minor amounts of foraminifera (Ehrmann & Mackensen, 1992) and good (minor evidence of dissolution or secondary calcite overgrowth) to excellent (no evidence of diagenetic alteration) preservation (Huber, 1991). However, any changes in carbonate mineralogy could cause the observed increase in $\delta^{26}Mg_{carbonate}$ towards the EOB (Figure 4) owing to a strong mineralogical control on Mg isotope fractionation between carbonates and solution, which has a negative offset following the sequence aragonite < high-Mg calcite < low-Mg calcite (Saenger & Wang, 2014). A change in the ratio of foraminifera to nannofossils could result in the observed $\delta^{26}Mg_{carbonate}$ variation (Figure 4) as foraminiferal calcite fractionates from seawater by >2‰ relative to nannofossils (Higgins & Schrag, 2015; Tipper, 2022). Alternatively, diagenesis, defined here as the recrystallization of high-Mg calcite or aragonite to a more

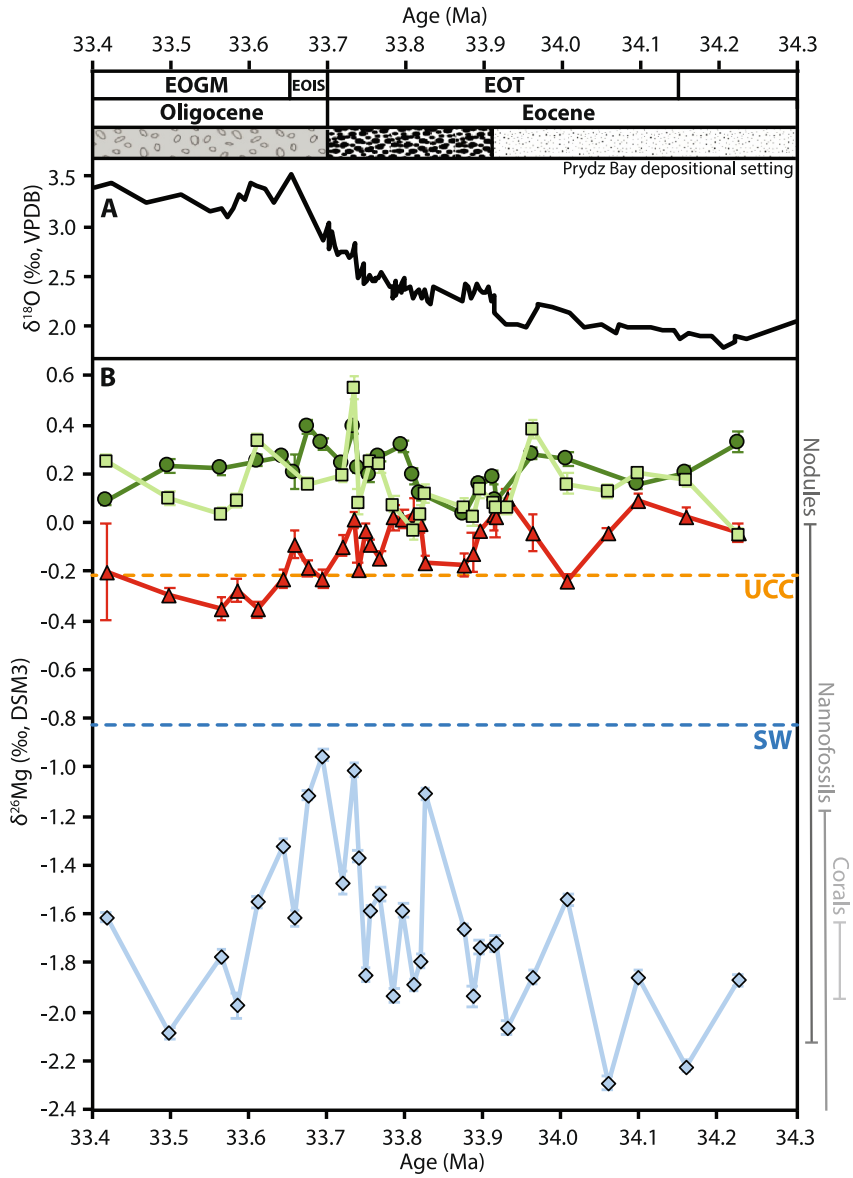

Figure 4. (a) Oxygen isotope record for Site 738 (Scher et al., 2011). (b) Magnesium isotope records for the carbonate (light blue diamonds), reactive (red triangles), residual (dark green circles), and fine (light green squares) fractions. The δ^{26}Mg data represents average values with 2SE uncertainty. Previously recorded values for the upper continental crust (W.-Y. Li et al., 2010), seawater (Foster et al., 2010), nodules (Rose-Koga & Albarède, 2010), carbonate-rich nannofossil oozes (Wombacher et al., 2011), and Late Eocene-Early Oligocene corals (Gothmann et al., 2017) are presented in b. Prydz Bay depositional settings are displayed running from left to right: (1) Diatomaceous mudstone and massive diamictite; (2) Prograding brown diamictites and mud intraclasts; and (3) Aggrading gray diamictite (Passchier et al., 2017).

thermodynamically stable low-Mg calcite, can influence $\delta^{26}Mg_{carbonate}$ through re-precipitation in a diagenetic fluid (He et al., 2020; Mavromatis et al., 2013; Tipper, 2022). In this section, we explore the potential influence of assemblage mixing and recrystallization on $\delta^{26}Mg_{carbonate}$.

Foraminiferal calcite is lacking in Sr when compared to nannofossil calcite and calcite/dolomite is lacking in Sr when compared to aragonite, allowing Sr/Ca to be used as an effective tracer of early marine diagenesis (Ahm et al., 2018; Edwards et al., 2015; Higgins et al., 2018). The carbonate fraction has Sr/Ca ratios of ~1.30 mmol/mol and δ^{26}Mg values of −1.67‰ ± 0.66‰ which is within the range of nannofossil oozes (Sr/Ca = 1.15–2.85 mmol/mol; δ^{26}Mg = −3.02‰ to −1.15‰) previously recorded (Figure 4; Ando et al., 2006; Wombacher et al., 2011). Constant Sr/Ca downcore and the absence of a relationship between Sr/Ca and $\delta^{26}Mg_{carbonate}$

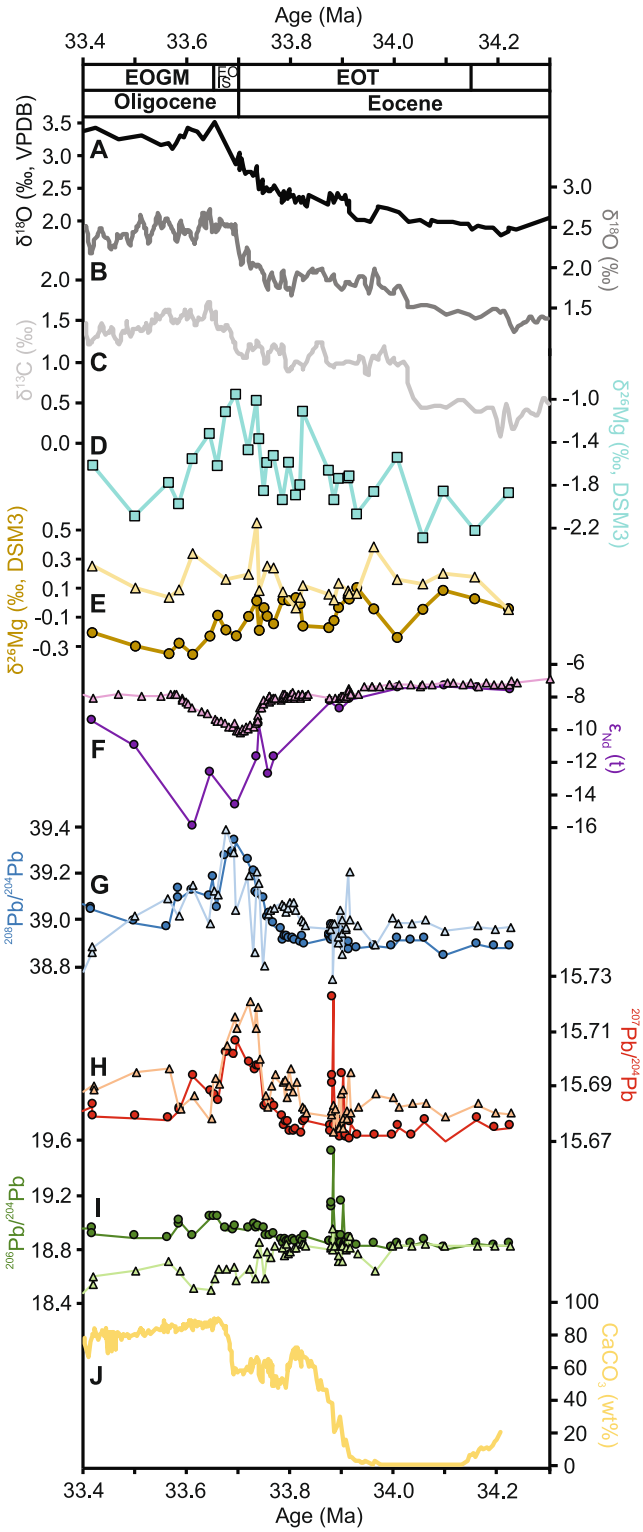

Figure 5.

(Figure 1f, Figure S1c in Supporting Information S1) indicate a change in mineralogy, for example, from nannofossil to foraminiferal calcite (Sr/Ca <1 mmol/mol; $\delta^{26}Mg = -4.91‰$ to $-4.40‰$) or aragonite (Sr/Ca ~10 mmol/mol; $\delta^{26}Mg = -1.95‰$ to $-1.64‰$) to calcite, is not responsible for the observed $\delta^{26}Mg_{carbonate}$ variability (Gothmann et al., 2017; He et al., 2020; Higgins & Schrag, 2015; Kinsman, 1969; Lowenstam, 1961). This is supported by no major faunal change across the EOT and a constant nannofossil/foraminifera ratio during this period (Ehrmann & Mackensen, 1992; Huber, 1991; Keller et al., 2014).

High-Mg calcite is characterized by non-unique Sr/Ca compared to aragonite and low-Mg calcite but is enriched in Li and Mg. This means that Li/Ca and Mg/Ca can be used to test the influence of high-Mg calcite recrystallization to low-Mg calcite on sediment geochemistry (Ahm et al., 2018; Higgins et al., 2018; Murphy et al., 2022). The carbonate fraction Li/Ca and Mg/Ca vary, respectively, from 5.0 to 33.1 μmol/mol and 6.0 to 11.3 mmol/mol (Figures 1b and 1c), suggesting recrystallization from high-Mg calcite to low-Mg calcite (Murphy et al., 2022) prior to ~33.75 Ma and after the EOB. The weak positive correlation between $\delta^{26}Mg_{carbonate}$ and Li/Ca and Mg/Ca (Figures S1a and S1b in Supporting Information S1) is therefore due to the precipitation of isotopically light secondary calcite (Higgins & Schrag, 2012; Saenger & Wang, 2014; Wombacher et al., 2011). Although we lack the Site 738 pore-fluid data needed to assess the impact of recrystallization on $\delta^{26}Mg_{carbonate}$, other deep-sea pelagic ooze studies have shown that recrystallization can only shift bulk carbonate values by 0.1‰–0.3‰ (Higgins & Schrag, 2012, 2015), which accounts for 8%–23% of the 1.3 ‰ $\delta^{26}Mg_{carbonate}$ range observed here.

Further insight into the influence of calcite recrystallization on $\delta^{26}Mg$ variability can be gleaned from Mn/Sr and Rb/Sr (Ahm et al., 2018; Cao et al., 2022; Fantle & Higgins, 2014; Higgins et al., 2018). As most diagenetic fluids are enriched in Mn when compared to Sr, any resulting recrystallization in this fluid would result in higher Mn/Sr (Brand & Veizer, 1980; Higgins et al., 2018). Both Mn/Sr and Rb/Sr ratios vary below the recommended thresholds for diagenetic alteration in carbonates of Mn/Sr ~ 3 mol/mol and Rb/Sr ~ 1 mol/mol (Ahm et al., 2018; Cao et al., 2022; Kaufman, 1994). These ratios display no significant correlation with $\delta^{26}Mg_{carbonate}$ values (Figures S1g and S1h in Supporting Information S1), suggesting minimal influence from marine diagenesis. This leaves us with two scenarios: (a) $\delta^{26}Mg_{carbonate}$ is recording the composition of nannofossils with no diagenetic alteration (based on Mn/Sr and Rb/Sr); or (b) $\delta^{26}Mg_{carbonate}$ is recording the composition of nannofossils with minor alterations from the recrystallization of low-Mg calcite (based on Li/Ca and Mg/Ca). Both scenarios require an additional source of heavy Mg to account for large isotope variation ($-1.67‰ \pm 0.66‰$) observed across the EOT, which are discussed in the following sections.

Figure 5. Proxy records covering the Late Eocene to Earliest Oligocene. (a) The oxygen isotope record for Site 738. A global compilation of oxygen (b) and carbon (c) isotope records (Westerhold et al., 2020). (d) Site 738 $\delta^{26}Mg_{carbonate}$ (e) $\delta^{26}Mg_{reactive}$ (yellow circles), and $\delta^{26}Mg_{fine}$ (yellow triangles) records. (f) Neodymium isotope records for the residual fraction (purple circles) and fish teeth (pink triangles) from Site 738 (Basak & Martin, 2013; Scher et al., 2011). The $^{208}Pb/^{204}Pb$ (g), $^{207}Pb/^{204}Pb$ (h), and $^{206}Pb/^{204}Pb$ (i) values for the residual (circles) and reactive (triangles) fraction from Site 738 (Basak & Martin, 2013). (j) Percent calcium carbonate from equatorial Pacific Site 1218 (Coxall et al., 2005).

4.1.2. Sediment Dissolution

The residual fraction is enriched in Mg (7,593 ± 4,046 μg/g) by one order of magnitude compared to the carbonate fraction (895 ± 556 μg/g), suggesting that even partial dissolution of detrital silicates could influence the δ^{26}Mg value of the carbonate fraction (Table S1). Other elements such as Al and Fe are also exceptionally high in silicates, allowing Al/Ca and Fe/Ca to be used to access silicate contamination (Cao et al., 2022; Pogge von Strandmann et al., 2013). Both ratios show a respective increase from ~120 to ~55 μmol/mol to maximum values of ~1,024 and ~137 μmol/mol between 33.76 Ma and the EOB (Figures 1d and 1e), which is weakly correlated with a shift in $\delta^{26}Mg_{carbonate}$ values towards higher EOB values (Figures S1d and S1e in Supporting Information S1). This could imply that partial dissolution of the residual silicates contributes Al, Fe, and ^{26}Mg to the carbonate fraction (Figure 4).

One method to correct for detrital contamination is to assume that all the Al in the carbonate fraction is sourced from the residual fraction. Magnesium isotope values from the carbonate fraction have been corrected for percent contribution from the fine fraction using the mass balance equation developed for Sr (Gutjahr et al., 2007) and Pb (Basak et al., 2011) isotopes:

$$[Mg]_{\%\ \text{contri. of fine Mg}} = \frac{[Al]_{carbonate}}{[Al]_{fine}} \quad (1)$$

$$[Mg]_{\text{fine contri. in carbonate fraction}} = [Mg]_{\%\ \text{contri. of fine Mg}} * [Mg]_{fine} \quad (2)$$

$$[Mg]_{\text{dissolved contri. in carbonate fraction}} = [Mg]_{carbonate} - [Mg]_{\text{fine contri. in carbonate fraction}} \quad (3)$$

$$\delta^{26}Mg_{corrected=} \frac{\left([Mg]_{carbonate} * \delta^{26}Mg_{carbonate}\right) - \left([Mg]_{\text{fine contri. in carbonate fraction}} * \delta^{26}Mg_{fine}\right)}{[Mg]_{\text{dissolved contri. in carbonate fraction}} \quad (4)$$

This technique likely overestimates the contribution of Mg from the fine fraction as it assumes that all Al is derived from the fine fraction and that there is complete dissolution of silicates as partial leaching would likely result in preferential release of ^{24}Mg (Huang et al., 2012; Liu et al., 2014; Teng, Li, Rudnick, & Gardner, 2010; Wimpenny et al., 2014). A comparison of $\delta^{26}Mg_{carbonate}$ and $\delta^{26}Mg_{corrected}$ shows sediment dissolution would be responsible for a maximum of 0.03 ‰ (Figure S3 in Supporting Information S1), indicating that sediment dissolution is not the source of isotopically heavy Mg to the carbonate fraction.

The REY content of the carbonate fraction can offer further insight into the impact of contamination from the detrital fraction and additional information concerning contamination from the reactive fraction. The HREEs in ambient seawater complex with carbonates while the LREEs are preferentially removed from solution via organic particle adsorption (Lee & Byrne, 1992; Sholkovitz et al., 1994). Meanwhile, oxygenated waters cause Ce(III) to be oxidized to Ce(IV), resulting in reduced Ce concentrations when compared to the other REEs (Sholkovitz & Shen, 1995). This behavior leads to HREE enrichment, high Y/Ho, and negative Ce anomalies in seawater, oxic porewaters, and associated carbonates (Smrzka et al., 2019) as observed in the carbonate fraction REY pattern recorded here (Figure 2a). On the other hand, the reactive fraction is comprised of Fe (oxyhydr)oxides with a typical Ce anomaly and MREE bulge and the residual fraction has a relatively flat REY profile indicative of recycled silicates (Figures 2b–2d; Basak et al., 2011; Gutjahr et al., 2007; Martin et al., 2010; Wilson et al., 2013).

Distinct REY profiles delineate the carbonate, reactive, and residual fraction within the HREE/LREE versus MREE/MREE* space (Figure 3; Haley et al., 2004; Martin et al., 2010). The enrichment of HREEs and absence of an MREE bulge gives the carbonate fraction a unique position close to previous acetic acid leached samples and seawater (Figure 3; De Baar et al., 1985; Lacan & Jeandel, 2005; Martin et al., 2010; Piepgras & Jacobsen, 1992; Zhang et al., 2008). The lack of a significant correlation between $\delta^{26}Mg_{carbonate}$ and HREE/LREE and MREE/MREE* suggests that dissolution of the residual or reactive fraction is not influencing the geochemistry of the carbonate fraction (Figure 3). This implies that the higher levels of Al, Fe, and ^{26}Mg from 33.76 Ma to the EOB are not supplied from sediment or Fe-Mn (oxyhydr)oxides dissolution and the associated increase in Al/Ca, Fe/Ca, and $\delta^{26}Mg_{carbonate}$ was caused by a different process.

4.1.3. Local Weathering Inputs to Seawater

The REY profiles and Sr/Ca of the carbonate fraction are compatible with nannofossils precipitating calcite from oxic surface waters (Figures 1f and 2a). The large oceanic reservoir of Mg means that the residence time is long (>10 Myr) compared to the mixing time of the oceans (~1 kyr) leading to a uniform seawater Mg isotope composition and concentration (Tipper, 2022). The short duration of the EOT (~790 kyr) relative to the oceanic residence time of Mg precludes the possibility of changes in seawater $\delta^{26}Mg$ as a driver of the $\delta^{26}Mg_{carbonate}$ variation recorded here. However, deviations from conservative Mg behavior in seawater are known to occur owing to processes such as ocean mixing, freshwater discharge, and ice melt (Krabbenhöft et al., 2010; Lebrato et al., 2020). Spatially heterogenous and highly variable Mg/Ca have been observed in river-influenced, shelf, neritic, and polar regions owing to variable Mg flux and other regional conditions (Blanco-Ameijeiras et al., 2012; Ingram et al., 1998; Lebrato et al., 2020). Local changes in ocean mixing and freshwater flux could therefore have influenced the $\delta^{26}Mg$ of surface waters and surface-dwelling organisms close to Antarctica.

During the EOT, the growth of the Antarctic ice sheet fundamentally reorganized ocean circulation by invigorating Antarctic Bottom Water formation and enhancing northward transport of Antarctic intermediate and surface waters (Goldner et al., 2014). This was associated with the expansion of the Antarctic ice sheet to coastal margins, which generated intense coastal sediment flux, focused in Prydz Bay, and a fivefold increase in iceberg calving rates (Pollard & DeConto, 2003; Van Breedam et al., 2022). During the Late Eocene, Site 738 was positioned close to the Antarctic continental shelf and upper slope where it received dense waters, terrigenous sediment, and ice-rafted-debris from the Antarctic coast (Huck et al., 2017; Scher et al., 2011, 2014). The calcareous biogenic component of Site 738 sediments records climatic fluctuations on the Antarctic continent and surrounding surface and intermediate waters, namely mixing between Antarctic Surface Water from the south and Subantarctic Surface Water from the north (Ehrmann & Mackensen, 1992; Huber, 1991). Antarctic Surface Water largely entrains glacial meltwater, which is exported hundreds of kilometers offshore through freshwater plumes, supporting phytoplankton blooms (Dierssen et al., 2002). The $\delta^{26}Mg_{carbonate}$ is therefore likely to record variations in the coastal freshwater signal emanating from melting glaciers along the Antarctic coastline, leading to local non-conservative Mg behavior (e.g., Lebrato et al., 2020) and dynamic isotope fluctuations on sub-million-year timescales.

Evidence to support this comes from radiogenic isotope studies of the Kerguelen Plateau. Due to the relatively short oceanic residence time of Nd (500–1,000 years) and Pb (30–400 years), Nd and Pb isotopes have become powerful tracers of water mass mixing and weathering inputs (Basak & Martin, 2013; Scher et al., 2011). Fish teeth records from Site 738 argue that an unrealistically large amount of Northern Component Water is needed to drive the observed ε_{Nd} excursion at the EOT (Figure 5d; Scher et al., 2011). Instead, the excursion requires glacial erosion of Antarctic bedrock and rapid chemical weathering of fresh mineral surfaces to release unradiogenic Nd, followed by rapid mixing of this Antarctic weathering flux with local water masses (Scher et al., 2011). This is consistent with covariation between Pb and Nd isotopes in the reactive and residual fractions, which suggests that Site 738 is recording local weathering inputs from Antarctica (Figures 5e–5g; Basak & Martin, 2013). These weathering inputs would have overwhelmed the advective signal for the short Pb, intermediate Nd, and long Mg oceanic residence times leading to a similar timing of isotope variability related to Antarctic glaciation (Figure 5a; Basak & Martin, 2013).

The $\delta^{18}O$ of seawater increases from ~33.75 Ma to the EOGM, driven by global cooling and expansion of the Antarctic ice sheet (Figures 5a and 5b). This is associated with a $^{208}Pb/^{204}Pb$, $^{207}Pb/^{204}Pb$, and $^{206}Pb/^{204}Pb$ excursion between ~33.80 Ma and the EOB and a ε_{Nd} excursion from ~33.76 Ma to the EOB (Figures 6f–6h) indicating a major increase in glacial erosion and chemical weathering of Antarctic bedrock (Basak & Martin, 2013; Scher et al., 2011). Chemical silicate weathering would have released cations such as Al, Fe, and Mg to the dissolved load, which would then be readily transported offshore in Antarctic Surface Water leading to the observed increase in Al/Ca, Fe/Ca, and $\delta^{26}Mg$ of surface-dwelling nannofossils (Figures 1b and 1c). Magnesium isotopes in the carbonate fraction are therefore likely responding to more intense chemical weathering of isotopically heavy silicates ($\delta^{26}Mg_{residual}$ = 0.23‰ ± 0.09‰) from Antarctica, leading to an increase in $\delta^{26}Mg_{carbonate}$ values at ~34 Ma, ~33.83 Ma, and between ~33.75 Ma and the EOB (Figure 4). Recorded $\delta^{26}Mg$ excursions of 0.7‰–0.9‰ are comparable to modern glacial system variability in West Greenland (0.7‰) and the Mackenzie Basin (1‰) which have similar catchment geology to Antarctica (Tipper et al., 2012; Wimpenny et al., 2011).

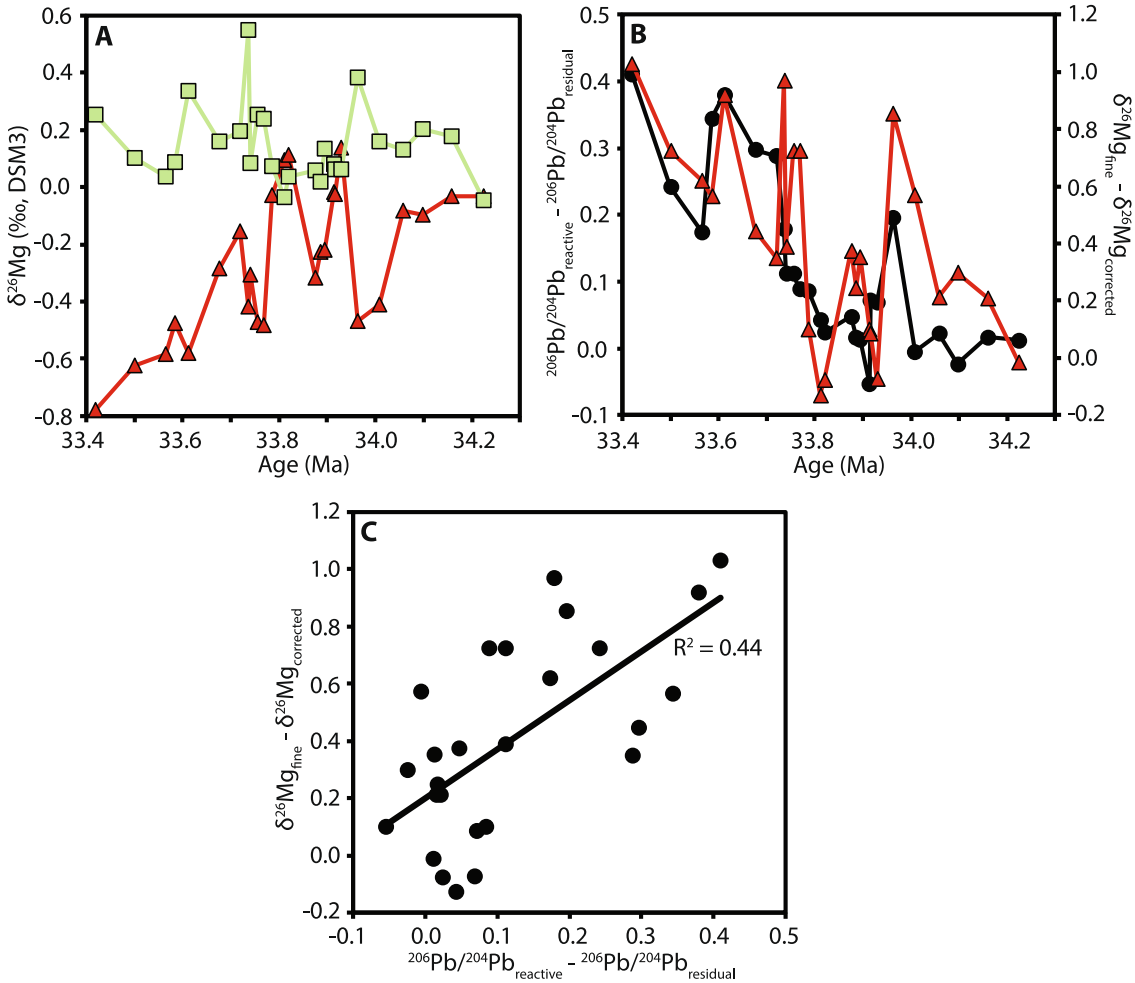

Figure 6. (a) Fine (green squares) and corrected reactive (red triangles) fraction $\delta^{26}Mg$ values. (b) The difference between the reactive and residual fraction for Pb (black circles; Basak & Martin, 2013) and Mg (red triangles; this study) isotopes. (c) The $^{206}Pb/^{204}Pb_{reactive} - {}^{206}Pb/^{204}Pb_{residual}$ versus $\delta^{26}Mg_{fine} - \delta^{26}Mg_{corrected}$ relationship ($p = <0.05$).

Lithium is incorporated into secondary weathering products such as clays and when compared to elements that are less sensitive to this process, such as Na, the Li/Na of riverine dissolved loads can be used to assess the production of secondary minerals (Dellinger et al., 2015; Millot et al., 2010). The Li/Na ratios of the carbonate fraction, a major signal of which is likely derived from the freshwater dissolved load entrained in Antarctic Surface Water, display a weak correlation with $\delta^{26}Mg$ suggesting that when clay formation is relatively low, and more Li is available in the dissolved load, $\delta^{26}Mg_{carbonate}$ values are high (Figure S1f in Supporting Information S1). This is compatible with field and laboratory studies which have shown ^{26}Mg is preferentially incorporated into Mg-clays (Teng, Li, Rudnick, & Gardner, 2010; Tipper et al., 2006, 2012). Variations in the $\delta^{26}Mg$ of the carbonate fraction therefore represent an increase in primary silicate dissolution of Antarctic bedrock, which is enriched in ^{26}Mg, and/or a reduction in secondary silicate production, which preferentially removes ^{26}Mg (Gothmann et al., 2017; Higgins & Schrag, 2015; Kasemann et al., 2014).

4.2. Evaluation of the Reactive Fraction as an Archive for the $\delta^{26}Mg$ of Seawater

The $\delta^{26}Mg$ of ferromanganese nodules overlaps with seawater values, presenting a potential archive for seawater $\delta^{26}Mg$ (Fu, 2020; Rose-Koga & Albarède, 2010). In this section, we assess the bottom water $\delta^{26}Mg$ archive potential of sediment ferromanganese coatings after considering diagenesis and sediment dissolution.

4.2.1. Hydrogenous Versus Diagenetic Source

Ferromanganese nodules from the Pacific and Atlantic oceans have $\delta^{26}Mg$ (−1.89‰ to −0.54‰) that scatter around seawater values due to the formation of hydrogenous vernadite minerals with a seawater composition followed by diagenetic transformation/formation of todorokite minerals from sediments (Rose-Koga & Albarède, 2010). The sources of hydrogenous and diagenetic Mg in ferromanganese coatings can be assessed using REY profiles and Mn/Fe. The REY budget of sedimentary foraminifera and calcareous nannofossils is dominated by reactive coatings derived from bottom waters (Palmer, 1985; Palmer & Elderfield, 1986; Roberts et al., 2012), as opposed to biogenic calcite, which precipitates from surface waters and likely comprises Fe and Mn (oxyhydr)oxides (Haley et al., 2004; Wilson et al., 2013). Scavenging of REYs via absorption onto the metal oxide surface has a higher affinity for Y and the MREEs (Smrzka et al., 2019). The reactive fraction REY patterns recorded here (Figure 2b) display the typical Ce anomalies and MREE bulge observed in reduced pore waters, marine sediments, and site 738 fish teeth, indicative of an Fe oxide source (Basak et al., 2011; Bayon et al., 2002; Haley et al., 2004; Kim et al., 2012; Martin et al., 2010; Scher et al., 2011; Wilson et al., 2013). A similar pattern is observed in Fe-Mn particles and nodules suggesting a potentially hydrogenous source that is precipitated from overlying oxic bottom waters (Figure 3; Basak et al., 2011; Jauhari & Pattan, 2017; Sherrell et al., 1999).

Hydrogenous ferromanganese nodules and reactive phases are generally enriched in Fe with Mn/Fe < 2.5 mol/mol, whereas diagenetic pore waters under oxic or suboxic conditions are enriched in Mn leading to Mn/Fe > 4 mol/mol (Basak et al., 2011; Menendez et al., 2019; Smrzka et al., 2019). The reactive fraction at Site 738 records Mn/Fe < 1.8 mmol/mol, indicating a hydrogenous Mg source. A weak negative correlation between Mn/Fe and $\delta^{26}Mg_{reactive}$ suggests minor diagenetic influence of $\delta^{26}Mg$ values at 33.79, 33.83, 3.57, and 33.42 Ma (Figure 1j, Figure S1i in Supporting Information S1). Removal of potentially altered samples has no bearing on the overall shape of the $\delta^{26}Mg_{reactive}$ curve which is similar to $\delta^{26}Mg_{fine}$, mimicking previous radiogenic isotope studies (Figures 4, 5g-i) that isolate a well-mixed seawater signal in equilibrium with the residual fraction (Basak & Martin, 2013). However, much like previous Pb and Nd isotope studies, $\delta^{26}Mg_{reactive}$ deviates from $\delta^{26}Mg_{fine}$ at ∼34.10 to 34.00 Ma, 33.93 to 33.83 Ma, and after 33.79 Ma, suggesting an additional input of ^{24}Mg (Figures 4, 5f-i).

4.2.2. Sediment Dissolution

The low Mg concentration in the reactive fraction (37 ± 38 μg/g) relative to the residual fraction (7,593 ± 4,046 μg/g) means even minor dissolution of detrital silicates could contribute significantly to the $\delta^{26}Mg_{reactive}$ record (Table S1). The reactive fraction displays a distinct MREE bulge represented by higher MREE/MREE* relative to the detrital fraction (Figure 3; Haley et al., 2004; Martin et al., 2010). The MREE/MREE* are negatively correlated with $\delta^{26}Mg_{reactive}$ implying that a flattening of the MREE bulge is caused by dissolution of the detrital fraction leading to higher $\delta^{26}Mg$ values ($R^2 = 0.27$, $p = <0.05$). One method to correct for detrital contamination is to assume that all the Al in the reactive fraction is sourced from the residual fraction. Using Eq1–4 but replacing $[Mg]_{carbonate}$ with $[Mg]_{reactive}$ and $\delta^{26}Mg_{carbonate}$ with $\delta^{26}Mg_{reactive}$ will provide a reactive fraction corrected for percent contribution from the fine fraction similar to previous studies of Sr (Gutjahr et al., 2007) and Pb (Basak et al., 2011) isotopes. A comparison of $\delta^{26}Mg_{fine}$ and $\delta^{26}Mg_{corrected}$ shows that the difference between $\delta^{26}Mg_{fine}$ and $\delta^{26}Mg_{reactive}$ at ∼34.00 Ma, 33.90 to 33.87 Ma, and after 33.79 Ma increases after correction, indicating sediment dissolution is not the source of light Mg to the reactive fraction (Figure 6a).

4.2.3. Local Carbonate Weathering as a Source of ^{24}Mg

The $^{206}Pb/^{204}Pb$ values for the reactive fraction from Site 738 diverge from the residual values requiring an additional input of ^{206}Pb that differs from the ^{207}Pb and ^{208}Pb sourced from enhanced silicate weathering of Antarctic Bedrock (Figure 5i; Basak & Martin, 2013). Phanerozoic carbonates likely have low Th and ^{235}U concentrations, which decay over time to become a source of easily weatherable ^{206}Pb (Basak & Martin, 2013). The difference between $\delta^{26}Mg_{fine}$ and $\delta^{26}Mg_{corrected}$ is weakly correlated with the difference between $^{206}Pb/^{204}Pb_{reactive}$ and $^{206}Pb/^{204}Pb_{residual}$, suggesting that carbonates represent the source of additional ^{24}Mg to the reactive fraction (Figures 6b and 6c). Large isotopic fractionation during the formation of carbonates leads to isotopically light values ($\delta^{26}Mg = -4.47$ to -1.69; Teng, 2017) that provide a source of ^{24}Mg to seawater during weathering (Higgins & Schrag, 2015; Tipper et al., 2006).

The chemistry of subglacial weathering outflow can be dominated by preferential weathering of trace carbonates in the underlying bedrock (Prestrud Anderson et al., 1997). Cambrian shallow marine carbonates make up 5%–10% of the exposed bedrock on Antarctica with the Shackleton Limestone outcropping along the southwest Antarctic shoreline (Elliot, 1975). East Antarctic Ice Sheet (EAIS) expansion and associated subglacial carbonate weathering under warm-based glaciers during the EOT could therefore be responsible for the observed decrease in $\delta^{26}Mg_{corrected}$ values (Basak & Martin, 2013). Alternatively, a glacial-hydro isostatic adjustment model suggests that the shelf area around the Prydz Bay region, close to Site 738, underwent rapid exposure during a relative sea-level drop of 50–100 m at the EOT (Stocchi et al., 2013), leading to greater weatherability of Antarctic shelf carbonates (Armstrong McKay et al., 2016; Merico et al., 2008). This study suggests that the reactive phase of marine sediments can record local variations in bottom water $\delta^{26}Mg$ but additional analysis of deep-sea sediments uninfluenced by weathering inputs is needed to assess if it can record well-mixed ocean values.

4.3. The Influence of Weathering Provenance and Intensity on the Residual Fraction

The $\delta^{26}Mg$ of silicates in the upper continental crust has a relatively narrow range of values (−0.3‰ to −0.1‰) but becomes fractionated during chemical weathering with the preferential retention of ^{26}Mg in weathering residues (<1.8‰; W.-Y. Li et al., 2010; Liu et al., 2014; Teng et al., 2016; Teng, Li, Ke, et al., 2010; Teng, Li, Rudnick, & Gardner, 2010). Previous studies have used this behavior in weathering residues to track past chemical weathering rates (Huang et al., 2016). In this section, we assess the potential for the residual fraction of marine sediments to trace the weathering of local material sourced from Antarctic bedrock at the EOT.

The elevated $\delta^{26}Mg_{residual}$ and $\delta^{26}Mg_{fine}$ values at 33.96 to 34.00, 33.89 to 33.91, and 33.68 to 33.80 Ma (Figure 4) occur during intense erosion events as indicated by Pb and Nd isotope values (Figures 5f–5i; Basak & Martin, 2013; Scher et al., 2011) and could therefore reflect an increase in weathering intensity of the same source material (i.e., a higher proportion of ^{26}Mg-rich weathering products relative to "fresh" bedrock) or a change in weathering provenance between two sources with different Mg isotope compositions. Elements such as Al, Fe, and Mg are considered more mobile relative to Ti and are lost during weathering leading to higher Al/Ti, Fe/Ti, and Mg/Ti in weathering products relative to the source rock (Young & Nesbitt, 1998). Residual Mg isotope values display no correlation with Al/Ti, Fe/Ti, and Mg/Ti (Figures S2a–S2c in Supporting Information S1), indicating that a shift from moderately to extremely weathered bedrock containing more weathering products such as clays is not responsible for the observed variation in $\delta^{26}Mg_{residual}$. This is supported by a lack of correlation with Li/Na, suggesting a limited impact from secondary mineral formation as previously discussed (Figure S2d in Supporting Information S1; Dellinger et al., 2015).

Residual Mg isotopes are weakly correlated with $^{208}Pb/^{204}Pb$ ($R^2 = 0.25$, $p = <0.05$) and $^{207}Pb/^{204}Pb$ ($R^2 = 0.28$, $p = <0.05$) and weakly negatively correlated with ε_{Nd} ($R^2 = 0.19$, $p = <0.05$) suggesting a change in weathering provenance is responsible for the observed increase in $\delta^{26}Mg_{residual}$ (Basak & Martin, 2013; Scher et al., 2011). Less radiogenic ε_{Nd} and more radiogenic $^{207}Pb/^{204}Pb$ values indicate a greater proportion of Precambrian basement rocks, which consist of granulite-facies intruded with granites and pegmatites, underlying Prydz Bay are being delivered to Site 738 along with ^{144}Nd and ^{207}Pb (Basak & Martin, 2013; Scher et al., 2011). This is consistent with a shift to weathered granite or granodiorite bedrock (Brewer et al., 2018) or more pristine Archean S-type potassic granites (R.-Y. Li et al., 2020), which are enriched in ^{26}Mg. This supports the notion that glacial expansion (increasing $\delta^{18}O$) removed the regolith and increased physical erosion of newly exposed material underlying a growing EAIS which was rapidly transported to the Kerguelen Plateau (Basak & Martin, 2013; Scher et al., 2011) leading to higher $\delta^{26}Mg_{residual}$ and $\delta^{26}Mg_{fine}$ values.

4.4. Implications for Global Climate Feedbacks

Late Eocene glaciers occupying the Antarctic interior were small and highly dynamic but coalesced to form a continental-scale EAIS at the EOT (DeConto et al., 2008; DeConto & Pollard, 2003). This change is represented by a depositional and temperature shift in Prydz Bay, downstream of a major EAIS drainage system, and $\delta^{18}O$ variation at Site 738: (a) Prior to 34.40 Ma, a lack of diamictites and a more equitable climate in Prydz Bay suggests ephemeral glaciers did not reach the coast; (b) gradual cooling and deposition of sandy diamictite in Prydz Bay indicates large-scale precursor glaciation coincident with a $\delta^{18}O$ increase from 34.20 Ma; (c) the arrival of the grounding-line onto the Prydz Bay continental shelf is marked by the delivery of brownish-gray diamictites and Step 1 and the EOIS between 33.90 and 33.70 Ma; (d) Silt-rich and clay-poor diamict

lithofacies indicate the presence of a grounded marine ice during the EOGM (Figure 4; Passchier et al., 2017; Rose et al., 2013; Tibbett et al., 2021; Tochilin et al., 2012).

The Mg isotope records presented here provide an insight into local Antarctic weathering processes during these events. Glaciations defined by positive $\delta^{18}O$ excursions at ~34 Ma, 33.93 to 33.91 Ma, and 33.82 to 33.70 Ma are associated with positive excursions in $\delta^{26}Mg_{residual}$ and $\delta^{26}Mg_{fine}$ representing the mechanical weathering and delivery of primary silicate bedrock sourced subglacially from the EAIS (Figure 4). Fine-grained material was chemically weathered by the large supply of subglacial meltwater from a warm-based EOT ice sheet (Vance et al., 2009; Zachos et al., 1999) leading to the release of ^{26}Mg and cations to the dissolved phase and an increase in $\delta^{26}Mg_{carbonate,}$ Al/Ca, and Fe/Ca (Figures 1 and 4). Transport of solid and dissolved material to the Kerguelen Plateau was rapid, preventing the formation of secondary silicates such as clays, which would otherwise decrease $\delta^{26}Mg_{carbonate}$ and Li/Na. Erosion stopped with the establishment of a cold-based ice sheet in Prydz Bay (Scher et al., 2011) leading to a reduction in physical and chemical subglacial weathering and therefore $\delta^{26}Mg_{residual}$, $\delta^{26}Mg_{fine}$, and $\delta^{26}Mg_{carbonate}$ values during the EOGM.

These findings support the notion that enhanced Antarctic silicate weatherability during the EOT converted atmospheric CO_2 to alkalinity for storage in the ocean (Basak & Martin, 2013; Ravizza & Peucker-Ehrenbrink, 2003; Scher et al., 2011). Reversal of this process through the formation of secondary silicates was limited, suggesting efficient CO_2 removal due to short fluid residence times and a weathering-limited regime (Dellinger et al., 2015; Pogge von Strandmann & Henderson, 2015). Silicate weathering would also have supplied nutrients to the Southern Ocean, stimulating primary productivity and further atmospheric CO_2 removal through organic carbon burial (Salamy & Zachos, 1999; Scher et al., 2011), as evidenced by transient variations in $\delta^{13}C$ (Figure 5c) and biogenic Ba (Rodrigues de Faria et al., 2024; Westerhold et al., 2020). Both mechanisms would have compounded atmospheric CO_2 drawdown, acting as a positive feedback on global climate (Armstrong McKay et al., 2016; Merico et al., 2008).

Increased concentrations of Ca^{2+} and alkalinity from silicate weathering likely contributed to an increase in ocean Ω and a deepening of the CCD. However, this was transient in nature and cannot explain the permanent stepwise shift from ~3.5 to 5 km across the EOT (Figure 5j; Armstrong McKay et al., 2016; Coxall et al., 2005). The $\delta^{26}Mg_{corrected}$ values record an enrichment of ^{24}Mg at ~34.0 Ma, ~33.9 Ma, and from ~33.8 Ma, indicating enhanced silicate weatherability was also associated with carbonate weathering, but also shows a stepwise trend that is not observed in other phases (Figure 4). The observed $\delta^{26}Mg_{corrected}$ shift from ~33.8 Ma coincides with a rapid sea-level fall of 50–100 m near Prydz Bay (Stocchi et al., 2013). This exposed shelf carbonates to weathering, delivering light Mg to Site 738 bottom waters, and reduced shelf carbonate burial, which was compensated by an increase in Ω and a deepening of the CCD (Figure 5j), supporting biogeochemical models (Armstrong McKay et al., 2016; Merico et al., 2008).

5. Conclusions

The Mg isotope composition of the carbonate, reactive, and residual/fine fractions compare well to values previously recorded for calcareous nannofossils, ferromanganese nodules, and weathered silicates, respectively. The carbonate fraction records past variation in surface water chemistry influenced by meltwater plumes with minimal influence from other fractions. The reactive fraction, on the other hand, records bottom water chemistry related to deep water formation along the Antarctic continental shelf, which is subsequently exported to the Kerguelen plateau. The residual/fine fraction represents a shift in silicate weathering provenance from recycled material along the Antarctic coastline to more pristine bedrock underlying expanding EAIS. In the future, the same leaching techniques need to be applied to deep sea sediments away from the influence of shelf water masses and local weathering inputs to assess their potential to record well-mixed seawater values in a similar manner to other paleoclimate archives.

The proximity of Site 738 to Antarctic glaciation and a major erosion episode overwhelmed the advective signal and long Mg mean ocean residence time, leading to local nonconservative Mg isotope behavior and a dynamic record of Antarctic weathering at the EOT. Together, the Mg isotope records presented here suggest that the expansion of the Antarctic ice sheet led to subglacial erosion and efficient chemical weathering of fresh silicate bedrock from the Antarctic interior. Rapid offshore transport of weathering products prevented the formation of clays leading to higher alkalinity and nutrient flux to the Southern Ocean and the removal of atmospheric CO_2. Local sea-level fall exposed Antarctic shelf carbonates to weathering, contributing to a deepening of the CCD

across the EOT. This study highlights how Mg isotopes, with careful site selection and sediment phase separation, can be used to reconstruct weathering regimes during dynamic sub-million-year climate events.

Conflict of Interest

The authors declare no conflicts of interest relevant to this study.

Data Availability Statement

The Site 738 element concentrations, rare-earth element and yttrium concentrations, PAAS-normalized rare-earth element and yttrium ratios, and magnesium isotope measurements used in this study are available in Tables S1–S4, respectively. The original data are also available at Zenodo via https://doi.org/10.5281/zenodo.13813977 under a Creative Commons Attribution license, which allows redistribution and reuse of the licensed work provided that the creator is appropriately credited (Sproson et al., 2025).

Acknowledgments

We thank E.E. Martin (University of Florida) for providing the sequential leaching protocol used in this study. We thank J. Kuroda (University of Tokyo) and K. Nagaishi (Marine Works Japan Ltd.) for assistance with REY oxide corrections and Mg isotope measurement, respectively. This research used samples and data provided by the Ocean Drilling Program (ODP) and International Ocean Discovery Program (IODP). Samples were provided by the Kochi Core Center (KCC) repository. We acknowledge a postdoctoral fellowship from the Japan Agency for Marine-Earth Science and Technology (Young Research Fellow to A. D.S.) and grants from the Japan Society for the Promotion of Science (22K14137 to A. D.S. and 21H01204 to T.Y.).

References

Ahm, A.-S. C., Bjerrum, C. J., Blättler, C. L., Swart, P. K., & Higgins, J. A. (2018). Quantifying early marine diagenesis in shallow-water carbonate sediments. *Geochimica et Cosmochimica Acta*, *236*, 140–159. https://doi.org/10.1016/j.gca.2018.02.042

Anagnostou, E., John, E. H., Edgar, K. M., Foster, G. L., Ridgwell, A., Inglis, G. N., et al. (2016). Changing atmospheric CO_2 concentration was the primary driver of early Cenozoic climate. *Nature*, *533*(7603), 380–384. https://doi.org/10.1038/nature17423

Ando, A., Kawahata, H., & Kakegawa, T. (2006). Sr/Ca ratios as indicators of varying modes of pelagic carbonate diagenesis in the ooze, chalk and limestone realms. *Sedimentary Geology*, *191*(1), 37–53. https://doi.org/10.1016/j.sedgeo.2006.01.003

Araoka, D., & Yoshimura, T. (2019). Rapid purification of alkali and alkaline-earth elements for isotope analysis (δ7Li, δ26Mg, 87Sr/86Sr, and δ88Sr) of rock samples using borate fusion followed by ion chromatography with a fraction collector system. *Analytical Sciences*, *18P509*.

Armstrong McKay, D. I., Tyrrell, T., & Wilson, P. A. (2016). Global carbon cycle perturbation across the Eocene-Oligocene climate transition. *Paleoceanography*, *31*(2), 311–329. https://doi.org/10.1002/2015pa002818

Axelsson, M. D., Rodushkin, I., Ingri, J., & Öhlander, B. (2002). Multielemental analysis of Mn–Fe nodules by ICP-MS: Optimisation of analytical method. *Analyst*, *127*(1), 76–82. https://doi.org/10.1039/B105706P

Basak, C., & Martin, E. E. (2013). Antarctic weathering and carbonate compensation at the Eocene–Oligocene transition. *Nature Geoscience*, *6*(2), 121–124. https://doi.org/10.1038/ngeo1707

Basak, C., Martin, E. E., & Kamenov, G. D. (2011). Seawater Pb isotopes extracted from Cenozoic marine sediments. *Chemical Geology*, *286*(3–4), 94–108. https://doi.org/10.1016/j.chemgeo.2011.04.007

Bayon, G., German, C. R., Boella, R. M., Milton, J. A., Taylor, R. N., & Nesbitt, R. W. (2002). An improved method for extracting marine sediment fractions and its application to Sr and Nd isotopic analysis. *Chemical Geology*, *187*(3), 179–199. https://doi.org/10.1016/S0009-2541(01)00416-8

Blanco-Ameijeiras, S., Lebrato, M., Stoll, H. M., Iglesias-Rodriguez, M., Méndez-Vicente, A., Sett, S., et al. (2012). Removal of organic magnesium in coccolithophore calcite. *Geochimica et Cosmochimica Acta*, *89*, 226–239. https://doi.org/10.1016/j.gca.2012.04.043

Bohaty, S. M., Zachos, J. C., & Delaney, M. L. (2012). Foraminiferal Mg/Ca evidence for southern ocean cooling across the Eocene–Oligocene transition. *Earth and Planetary Science Letters*, *317*, 251–261. https://doi.org/10.1016/j.epsl.2011.11.037

Brand, U., & Veizer, J. (1980). Chemical diagenesis of a multicomponent carbonate system; 1, Trace elements. *Journal of Sedimentary Research*, *50*(4), 1219–1236. https://doi.org/10.1306/212F7BB7-2B24-11D7-8648000102C1865D

Brewer, A., Teng, F.-Z., & Dethier, D. (2018). Magnesium isotope fractionation during granite weathering. *Chemical Geology*, *501*, 95–103. https://doi.org/10.1016/j.chemgeo.2018.10.013

Cao, C., Bataille, C. P., Song, H., Saltzman, M. R., Tierney Cramer, K., Wu, H., et al. (2022). Persistent late Permian to Early Triassic warmth linked to enhanced reverse weathering. *Nature Geoscience*, *15*(10), 832–838. https://doi.org/10.1038/s41561-022-01009-x

Coxall, H. K., Wilson, P. A., Pälike, H., Lear, C. H., & Backman, J. (2005). Rapid stepwise onset of Antarctic glaciation and deeper calcite compensation in the Pacific Ocean. *Nature*, *433*(7021), 53–57. https://doi.org/10.1038/nature03135

De Baar, H. J. W., Bacon, M. P., Brewer, P. G., & Bruland, K. W. (1985). Rare earth elements in the Pacific and Atlantic Oceans. *Geochimica et Cosmochimica Acta*, *49*(9), 1943–1959. https://doi.org/10.1016/0016-7037(85)90089-4

DeConto, R. M., & Pollard, D. (2003). Rapid Cenozoic glaciation of Antarctica induced by declining atmospheric CO_2. *Nature*, *421*(6920), 245–249. https://doi.org/10.1038/nature01290

DeConto, R. M., Pollard, D., Wilson, P. A., Pälike, H., Lear, C. H., & Pagani, M. (2008). Thresholds for Cenozoic bipolar glaciation. *Nature*, *455*(7213), 652–656. https://doi.org/10.1038/nature07337

Dellinger, M., Gaillardet, J., Bouchez, J., Calmels, D., Louvat, P., Dosseto, A., et al. (2015). Riverine Li isotope fractionation in the Amazon River basin controlled by the weathering regimes. *Geochimica et Cosmochimica Acta*, *164*, 71–93. https://doi.org/10.1016/j.gca.2015.04.042

Dierssen, H. M., Smith, R. C., & Vernet, M. (2002). Glacial meltwater dynamics in coastal waters west of the Antarctic peninsula. *Proceedings of the National Academy of Sciences*, *99*(4), 1790–1795. https://doi.org/10.1073/pnas.032206999

Edwards, C. T., Saltzman, M. R., Leslie, S. A., Bergström, S. M., Sedlacek, A. R. C., Howard, A., et al. (2015). Strontium isotope (87Sr/86Sr) stratigraphy of Ordovician bulk carbonate: Implications for preservation of primary seawater values. *GSA Bulletin*, *127*(9–10), 1275–1289. https://doi.org/10.1130/B31149.1

Ehrmann, W. U., & Mackensen, A. (1992). Sedimentological evidence for the formation of an East Antarctic ice sheet in Eocene/Oligocene time. *Palaeogeography, Palaeoclimatology, Palaeoecology*, *93*(1), 85–112. https://doi.org/10.1016/0031-0182(92)90185-8

Elliot, D. H. (1975). Tectonics of Antarctica: A review.

Eom, J., Yoshimura, T., Akizawa, N., Wakaki, S., Ishikawa, T., Takazawa, E., et al. (2022). The magnesium isotopic compositions of the crust and mantle: A study on the Oman ophiolite. *Chemical Geology*, *606*, 120969. https://doi.org/10.1016/j.chemgeo.2022.120969

Fantle, M. S., & Higgins, J. (2014). The effects of diagenesis and dolomitization on Ca and Mg isotopes in marine platform carbonates: Implications for the geochemical cycles of Ca and Mg. *Geochimica et Cosmochimica Acta*, *142*, 458–481. https://doi.org/10.1016/j.gca.2014.07.025

Foster, G., Pogge von Strandmann, P. A., & Rae, J. W. B. (2010). Boron and magnesium isotopic composition of seawater. *Geochemistry, Geophysics, Geosystems*, *11*(8), Q08015. https://doi.org/10.1029/2010gc003201

Fu, Y. (2020). Non-traditional stable isotope geochemistry of marine ferromanganese crusts and nodules. *Journal of Oceanography*, *76*(2), 71–89. https://doi.org/10.1007/s10872-019-00534-5

Fukamachi, Y., Rintoul, S. R., Church, J. A., Aoki, S., Sokolov, S., Rosenberg, M. A., & Wakatsuchi, M. (2010). Strong export of Antarctic Bottom Water east of the Kerguelen plateau. *Nature Geoscience*, *3*(5), 327–331. https://doi.org/10.1038/ngeo842

Galy, A., Bar-Matthews, M., Halicz, L., & O'Nions, R. K. (2002). Mg isotopic composition of carbonate: Insight from speleothem formation. *Earth and Planetary Science Letters*, *201*(1), 105–115. https://doi.org/10.1016/s0012-821x(02)00675-1

Goldner, A., Herold, N., & Huber, M. (2014). Antarctic glaciation caused ocean circulation changes at the Eocene–Oligocene transition. *Nature*, *511*(7511), 574–577. https://doi.org/10.1038/nature13597

Gothmann, A. M., Stolarski, J., Adkins, J. F., & Higgins, J. A. (2017). A Cenozoic record of seawater Mg isotopes in well-preserved fossil corals. *Geology*, *45*(11), 1039–1042. https://doi.org/10.1130/g39418.1

Gradstein, F. M. (2012). *The geologic time scale 2012*. Elsevier.

Griffith, E. M., Paytan, A., Eisenhauer, A., Bullen, T. D., & Thomas, E. (2011). Seawater calcium isotope ratios across the Eocene-Oligocene transition. *Geology*, *39*(7), 683–686. https://doi.org/10.1130/g31872.1

Gutjahr, M., Frank, M., Stirling, C. H., Klemm, V., van de Flierdt, T., & Halliday, A. N. (2007). Reliable extraction of a deepwater trace metal isotope signal from Fe–Mn oxyhydroxide coatings of marine sediments. *Chemical Geology*, *242*(3), 351–370. https://doi.org/10.1016/j.chemgeo.2007.03.021

Haley, B. A., Klinkhammer, G. P., & McManus, J. (2004). Rare earth elements in pore waters of marine sediments. *Geochimica et Cosmochimica Acta*, *68*(6), 1265–1279. https://doi.org/10.1016/j.gca.2003.09.012

He, R., Ning, M., Huang, K., Ma, H., & Shen, B. (2020). Mg isotopic systematics during early diagenetic aragonite-calcite transition: Insights from the Key Largo Limestone. *Chemical Geology*, *558*, 119876. https://doi.org/10.1016/j.chemgeo.2020.119876

Higgins, J. A., Blättler, C. L., Lundstrom, E. A., Santiago-Ramos, D. P., Akhtar, A. A., Crüger Ahm, A. S., et al. (2018). Mineralogy, early marine diagenesis, and the chemistry of shallow-water carbonate sediments. *Geochimica et Cosmochimica Acta*, *220*, 512–534. https://doi.org/10.1016/j.gca.2017.09.046

Higgins, J. A., & Schrag, D. P. (2010). Constraining magnesium cycling in marine sediments using magnesium isotopes. *Geochimica et Cosmochimica Acta*, *74*(17), 5039–5053. https://doi.org/10.1016/j.gca.2010.05.019

Higgins, J. A., & Schrag, D. P. (2012). Records of Neogene seawater chemistry and diagenesis in deep-sea carbonate sediments and pore fluids. *Earth and Planetary Science Letters*, *357–358*, 386–396. https://doi.org/10.1016/j.epsl.2012.08.030

Higgins, J. A., & Schrag, D. P. (2015). The Mg isotopic composition of Cenozoic seawater–evidence for a link between Mg-clays, seawater Mg/Ca, and climate. *Earth and Planetary Science Letters*, *416*, 73–81. https://doi.org/10.1016/j.epsl.2015.01.003

Hill, D. J., Haywood, A. M., Valdes, P. J., Francis, J. E., Lunt, D. J., Wade, B. S., & Bowman, V. C. (2013). Paleogeographic controls on the onset of the Antarctic circumpolar current. *Geophysical Research Letters*, *40*(19), 5199–5204. https://doi.org/10.1002/grl.50941

Huang, K.-J., Teng, F.-Z., Shen, B., Xiao, S., Lang, X., Ma, H.-R., et al. (2016). Episode of intense chemical weathering during the termination of the 635 Ma Marinoan glaciation. *Proceedings of the National Academy of Sciences*, *113*(52), 14904–14909. https://doi.org/10.1073/pnas.1607712113

Huang, K.-J., Teng, F.-Z., Wei, G.-J., Ma, J.-L., & Bao, Z.-Y. (2012). Adsorption- and desorption-controlled magnesium isotope fractionation during extreme weathering of basalt in Hainan Island, China. *Earth and Planetary Science Letters*, *359–360*, 73–83. https://doi.org/10.1016/j.epsl.2012.10.007

Huber, B. (1991). Paleogene and early Neogene planktonic foraminifer biostratigraphy of Sites 738 and 744, Kerguelen Plateau (southern Indian Ocean). In *Proceedings of the Ocean Drilling Program, scientific results*.

Huck, C. E., van de Flierdt, T., Bohaty, S. M., & Hammond, S. J. (2017). Antarctic climate, Southern Ocean circulation patterns, and deep water formation during the Eocene. *Paleoceanography*, *32*(7), 674–691. https://doi.org/10.1002/2017pa003135

Hutchinson, D. K., Coxall, H. K., Lunt, D. J., Steinthorsdottir, M., De Boer, A. M., Baatsen, M., et al. (2021). The Eocene–Oligocene transition: A review of marine and terrestrial proxy data, models and model–data comparisons. *Climate of the Past*, *17*(1), 269–315. https://doi.org/10.5194/cp-17-269-2021

Ingram, B., De Deckker, P., Chivas, A., Conrad, M., & Byrne, A. (1998). Stable isotopes, Sr/Ca, and Mg/Ca in biogenic carbonates from Petaluma Marsh, northern California, USA. *Geochimica et Cosmochimica Acta*, *62*(19–20), 3229–3237. https://doi.org/10.1016/s0016-7037(98)00240-3

Jauhari, P., & Pattan, J. (2017). Ferromanganese nodules from the central Indian Ocean basin. In *Handbook of marine mineral deposits* (pp. 171–196). Routledge.

Kasemann, S. A., Pogge von Strandmann, P. A. E., Prave, A. R., Fallick, A. E., Elliott, T., & Hoffmann, K.-H. (2014). Continental weathering following a Cryogenian glaciation: Evidence from calcium and magnesium isotopes. *Earth and Planetary Science Letters*, *396*, 66–77. https://doi.org/10.1016/j.epsl.2014.03.048

Kaufman, J. (1994). Numerical models of fluid flow in carbonate platforms; implications for dolomitization. *Journal of Sedimentary Research*, *64*(1a), 128–139. https://doi.org/10.1306/D4267D2F-2B26-11D7-8648000102C1865D

Keller, G., MacLeod, N., & Barrera, E. (2014). 11. Eocene-Oligocene faunal turnover in planktic Foraminifera, and antarctic glaciation. *Eocene-Oligocene climatic and biotic evolution*, 218–244.

Kennett, J. P. (1977). Cenozoic evolution of Antarctic glaciation, the circum-Antarctic Ocean, and their impact on global paleoceanography. *Journal of Geophysical Research*, *82*(27), 3843–3860. https://doi.org/10.1029/jc082i027p03843

Kim, J.-H., Torres, M. E., Haley, B. A., Kastner, M., Pohlman, J. W., Riedel, M., & Lee, Y.-J. (2012). The effect of diagenesis and fluid migration on rare earth element distribution in pore fluids of the northern Cascadia accretionary margin. *Chemical Geology*, *291*, 152–165. https://doi.org/10.1016/j.chemgeo.2011.10.010

Kinsman, D. J. J. (1969). Interpretation of Sr (super +2) concentrations in carbonate minerals and rocks. *Journal of Sedimentary Research*, *39*(2), 486–508. https://doi.org/10.1306/74D71CB7-2B21-11D7-8648000102C1865D

Krabbenhöft, A., Eisenhauer, A., Böhm, F., Vollstaedt, H., Fietzke, J., Liebetrau, V., & Horn, C. (2010). Constraining the marine strontium budget with natural strontium isotope fractionations (87Sr/86Sr*, δ88/86Sr) of carbonates, hydrothermal solutions and river waters. *Geochimica et Cosmochimica Acta*, *74*(14), 4097–4109.

Lacan, F., & Jeandel, C. (2005). Acquisition of the neodymium isotopic composition of the North Atlantic Deep Water. *Geochemistry, Geophysics, Geosystems*, *6*(12), Q12008. https://doi.org/10.1029/2005GC000956

Lear, C. H., Bailey, T. R., Pearson, P. N., Coxall, H. K., & Rosenthal, Y. (2008). Cooling and ice growth across the Eocene-Oligocene transition. *Geology*, *36*(3), 251–254. https://doi.org/10.1130/g24584a.1

Lear, C. H., & Rosenthal, Y. (2006). Benthic foraminiferal Li/Ca: Insights into Cenozoic seawater carbonate saturation state. *Geology*, *34*(11), 985–988. https://doi.org/10.1130/g22792a.1

Lebrato, M., Garbe-Schönberg, D., Müller, M. N., Blanco-Ameijeiras, S., Feely, R. A., Lorenzoni, L., et al. (2020). Global variability in seawater Mg: Ca and Sr: Ca ratios in the modern ocean. *Proceedings of the National Academy of Sciences*, *117*(36), 22281–22292. https://doi.org/10.1073/pnas.1918943117

Lee, J. H., & Byrne, R. H. (1992). Examination of comparative rare earth element complexation behavior using linear free-energy relationships. *Geochimica et Cosmochimica Acta*, *56*(3), 1127–1137. https://doi.org/10.1016/0016-7037(92)90050-S

Li, R.-Y., Ke, S., Li, S., Song, S., Wang, C., & Liu, C. (2020). Origins of two types of Archean potassic granite constrained by Mg isotopes and statistical geochemistry: Implications for continental crustal evolution. *Lithos*, *368*, 105570. https://doi.org/10.1016/j.lithos.2020.105570

Li, W.-Y., Teng, F.-Z., Ke, S., Rudnick, R. L., Gao, S., Wu, F.-Y., & Chappell, B. W. (2010). Heterogeneous magnesium isotopic composition of the upper continental crust. *Geochimica et Cosmochimica Acta*, *74*(23), 6867–6884. https://doi.org/10.1016/j.gca.2010.08.030

Liu, X.-M., Teng, F.-Z., Rudnick, R. L., McDonough, W. F., & Cummings, M. L. (2014). Massive magnesium depletion and isotope fractionation in weathered basalts. *Geochimica et Cosmochimica Acta*, *135*, 336–349. https://doi.org/10.1016/j.gca.2014.03.028

Lowenstam, H. A. (1961). Mineralogy, O18/O16 ratios, and strontium and magnesium contents of recent and fossil brachiopods and their bearing on the history of the Oceans. *The Journal of Geology*, *69*(3), 241–260. https://doi.org/10.1086/626740

Lyle, M., Barron, J., Bralower, T. J., Huber, M., Olivarez Lyle, A., Ravelo, A. C., et al. (2008). Pacific Ocean and Cenozoic evolution of climate. *Reviews of Geophysics*, *46*(2). https://doi.org/10.1029/2005rg000190

Martin, E. E., Blair, S. W., Kamenov, G. D., Scher, H. D., Bourbon, E., Basak, C., & Newkirk, D. N. (2010). Extraction of Nd isotopes from bulk deep sea sediments for paleoceanographic studies on Cenozoic time scales. *Chemical Geology*, *269*(3–4), 414–431. https://doi.org/10.1016/j.chemgeo.2009.10.016

Mavromatis, V., Gautier, Q., Bosc, O., & Schott, J. (2013). Kinetics of Mg partition and Mg stable isotope fractionation during its incorporation in calcite. *Geochimica et Cosmochimica Acta*, *114*, 188–203. https://doi.org/10.1016/j.gca.2013.03.024

Menendez, A., James, R. H., Lichtschlag, A., Connelly, D., & Peel, K. (2019). Controls on the chemical composition of ferromanganese nodules in the Clarion-Clipperton Fracture Zone, eastern equatorial Pacific. *Marine Geology*, *409*, 1–14. https://doi.org/10.1016/j.margeo.2018.12.004

Merico, A., Tyrrell, T., & Wilson, P. A. (2008). Eocene/Oligocene ocean de-acidification linked to Antarctic glaciation by sea-level fall. *Nature*, *452*(7190), 979–982. https://doi.org/10.1038/nature06853

Millot, R., Vigier, N., & Gaillardet, J. (2010). Behaviour of lithium and its isotopes during weathering in the Mackenzie Basin, Canada. *Geochimica et Cosmochimica Acta*, *74*(14), 3897–3912. https://doi.org/10.1016/j.gca.2010.04.025

Murphy, J. G., Ahm, A.-S. C., Swart, P. K., & Higgins, J. A. (2022). Reconstructing the lithium isotopic composition (δ7Li) of seawater from shallow marine carbonate sediments. *Geochimica et Cosmochimica Acta*, *337*, 140–154. https://doi.org/10.1016/j.gca.2022.09.019

Orsi, A. H., Johnson, G. C., & Bullister, J. L. (1999). Circulation, mixing, and production of Antarctic Bottom Water. *Progress in Oceanography*, *43*(1), 55–109. https://doi.org/10.1016/S0079-6611(99)00004-X

Pagani, M., Huber, M., Liu, Z., Bohaty, S. M., Henderiks, J., Sijp, W., et al. (2011). The role of carbon dioxide during the onset of Antarctic glaciation. *Science*, *334*(6060), 1261–1264. https://doi.org/10.1126/science.1203909

Palmer, M. R. (1985). Rare earth elements in Foraminifera tests. *Earth and Planetary Science Letters*, *73*(2), 285–298. https://doi.org/10.1016/0012-821X(85)90077-9

Palmer, M. R., & Elderfield, H. (1986). Rare earth elements and neodymium isotopes in ferromanganese oxide coatings of Cenozoic Foraminifera from the Atlantic Ocean Cambridge Earth Sciences Series, Contribution No. 651. *Geochimica et Cosmochimica Acta*, *50*(3), 409–417. https://doi.org/10.1016/0016-7037(86)90194-8

Passchier, S., Ciarletta, D. J., Miriagos, T. E., Bijl, P. K., & Bohaty, S. M. (2017). An antarctic stratigraphic record of stepwise ice growth through the Eocene-Oligocene transition. *Bulletin*, *129*(3–4), 318–330. https://doi.org/10.1130/b31482.1

Pearson, P. N., Foster, G. L., & Wade, B. S. (2009). Atmospheric carbon dioxide through the Eocene–Oligocene climate transition. *Nature*, *461*(7267), 1110–1113. https://doi.org/10.1038/nature08447

Piepgras, D. J., & Jacobsen, S. B. (1992). The behavior of rare earth elements in seawater: Precise determination of variations in the North Pacific water column. *Geochimica et Cosmochimica Acta*, *56*(5), 1851–1862. https://doi.org/10.1016/0016-7037(92)90315-A

Pogge von Strandmann, P. A., Forshaw, J., & Schmidt, D. N. (2014). Modern and Cenozoic records of seawater magnesium from foraminiferal Mg isotopes. *Biogeosciences*, *11*(18), 5155–5168. https://doi.org/10.5194/bg-11-5155-2014

Pogge von Strandmann, P. A. E. (2008). Precise magnesium isotope measurements in core top planktic and benthic Foraminifera. *Geochemistry, Geophysics, Geosystems*, *9*(12), Q12015. https://doi.org/10.1029/2008GC002209

Pogge von Strandmann, P. A. E., & Henderson, G. M. (2015). The Li isotope response to mountain uplift. *Geology*, *43*(1), 67–70. https://doi.org/10.1130/g36162.1

Pogge von Strandmann, P. A. E., Jenkyns, H. C., & Woodfine, R. G. (2013). Lithium isotope evidence for enhanced weathering during Oceanic Anoxic Event 2. *Nature Geoscience*, *6*(8), 668–672. https://doi.org/10.1038/ngeo1875

Pollard, D., & DeConto, R. M. (2003). Antarctic ice and sediment flux in the Oligocene simulated by a climate–ice sheet–sediment model. *Palaeogeography, Palaeoclimatology, Palaeoecology*, *198*(1–2), 53–67. https://doi.org/10.1016/s0031-0182(03)00394-8

Prestrud Anderson, S., Drever, J. I., & Humphrey, N. F. (1997). Chemical weathering in glacial environments. *Geology*, *25*(5), 399–402. https://doi.org/10.1130/0091-7613(1997)025<0399:CWIGE>2.3.CO;2

Ravizza, G., & Peucker-Ehrenbrink, B. (2003). The marine 187Os/188Os record of the Eocene–Oligocene transition: The interplay of weathering and glaciation. *Earth and Planetary Science Letters*, *210*(1–2), 151–165. https://doi.org/10.1016/s0012-821x(03)00137-7

Rea, D. K., & Lyle, M. W. (2005). Paleogene calcite compensation depth in the eastern subtropical Pacific: Answers and questions. *Paleoceanography*, *20*(1), 1–9. https://doi.org/10.1029/2004pa001064

Roberts, N. L., Piotrowski, A. M., Elderfield, H., Eglinton, T. I., & Lomas, M. W. (2012). Rare earth element association with Foraminifera. *Geochimica et Cosmochimica Acta*, *94*, 57–71. https://doi.org/10.1016/j.gca.2012.07.009

Rodrigues de Faria, G., Lazarus, D., Renaudie, J., Stammeier, J., Özen, V., & Struck, U. (2024). Late Eocene to early Oligocene productivity events in the proto-Southern Ocean and correlation to climate change. *Climate of the Past*, *20*(6), 1327–1348. https://doi.org/10.5194/cp-20-1327-2024

Rose, K. C., Ferraccioli, F., Jamieson, S. S., Bell, R. E., Corr, H., Creyts, T. T., et al. (2013). Early East Antarctic ice sheet growth recorded in the landscape of the Gamburtsev Subglacial Mountains. *Earth and Planetary Science Letters*, *375*, 1–12. https://doi.org/10.1016/j.epsl.2013.03.053

Rose-Koga, E. F., & Albarède, F. (2010). A data brief on magnesium isotope compositions of marine calcareous sediments and ferromanganese nodules. *Geochemistry, Geophysics, Geosystems*, *11*(3). https://doi.org/10.1029/2009GC002899

Saenger, C., & Wang, Z. (2014). Magnesium isotope fractionation in biogenic and abiogenic carbonates: Implications for paleoenvironmental proxies. *Quaternary Science Reviews*, *90*, 1–21. https://doi.org/10.1016/j.quascirev.2014.01.014

Salamy, K. A., & Zachos, J. C. (1999). Latest Eocene–Early Oligocene climate change and Southern Ocean fertility: Inferences from sediment accumulation and stable isotope data. *Palaeogeography, Palaeoclimatology, Palaeoecology*, *145*(1–3), 61–77. https://doi.org/10.1016/s0031-0182(98)00093-5

Scher, H. D., Bohaty, S. M., Smith, B. W., & Munn, G. H. (2014). Isotopic interrogation of a suspected late Eocene glaciation. *Paleoceanography*, *29*(6), 628–644. https://doi.org/10.1002/2014pa002648

Scher, H. D., Bohaty, S. M., Zachos, J. C., & Delaney, M. L. (2011). Two-stepping into the icehouse: East Antarctic weathering during progressive ice-sheet expansion at the Eocene–Oligocene transition. *Geology*, *39*(4), 383–386. https://doi.org/10.1130/g31726.1

Scher, H. D., Whittaker, J. M., Williams, S. E., Latimer, J. C., Kordesch, W. E., & Delaney, M. L. (2015). Onset of Antarctic Circumpolar Current 30 million years ago as Tasmanian Gateway aligned with westerlies. *Nature*, *523*(7562), 580–583. https://doi.org/10.1038/nature14598

Shalev, N., Bontognali, T. R., & Vance, D. (2021). Sabkha dolomite as an archive for the magnesium isotope composition of seawater. *Geology*, *49*(3), 253–257. https://doi.org/10.1130/g47973.1

Shalev, N., Lazar, B., Halicz, L., & Gavrieli, I. (2021). The Mg isotope signature of marine Mg-evaporites. *Geochimica et Cosmochimica Acta*, *301*, 30–47. https://doi.org/10.1016/j.gca.2021.02.032

Sherrell, R. M., Field, M. P., & Ravizza, G. (1999). Uptake and fractionation of rare earth elements on hydrothermal plume particles at 9°45′N, East Pacific Rise. *Geochimica et Cosmochimica Acta*, *63*(11), 1709–1722. https://doi.org/10.1016/S0016-7037(99)00182-9

Sholkovitz, E., & Shen, G. T. (1995). The incorporation of rare earth elements in modern coral. *Geochimica et Cosmochimica Acta*, *59*(13), 2749–2756. https://doi.org/10.1016/0016-7037(95)00170-5

Sholkovitz, E. R., Landing, W. M., & Lewis, B. L. (1994). Ocean particle chemistry: The fractionation of rare earth elements between suspended particles and seawater. *Geochimica et Cosmochimica Acta*, *58*(6), 1567–1579. https://doi.org/10.1016/0016-7037(94)90559-2

Smrzka, D., Zwicker, J., Bach, W., Feng, D., Himmler, T., Chen, D., & Peckmann, J. (2019). The behavior of trace elements in seawater, sedimentary pore water, and their incorporation into carbonate minerals: A review. *Facies*, *65*(4), 41. https://doi.org/10.1007/s10347-019-0581-4

Speer, K. G., & Forbes, A. (1994). A deep western boundary current in the South Indian basin. *Deep Sea Research Part I: Oceanographic Research Papers*, *41*(9), 1289–1303. https://doi.org/10.1016/0967-0637(94)90098-1

Sproson, A., Yoshimura, T., Shigeyuki, W., Aze, T., Yokoyama, Y., Ishikawa, T., & Ohkouchi, N. (2025). ODP Leg 119 Site 738 magnesium isotope and major, trace, and rare-earth element data sets. *Zenodo*. https://doi.org/10.5281/zenodo.13813977

Stocchi, P., Escutia, C., Houben, A. J., Vermeersen, B. L., Bijl, P. K., Brinkhuis, H., et al. (2013). Relative sea-level rise around East Antarctica during Oligocene glaciation. *Nature Geoscience*, *6*(5), 380–384. https://doi.org/10.1038/ngeo1783

Taylor, S. R., & McLennan, S. M. (1985). The continental crust: Its composition and evolution.

Teng, F.-Z. (2017). Magnesium isotope geochemistry. *Reviews in Mineralogy and Geochemistry*, *82*(1), 219–287. https://doi.org/10.2138/rmg.2017.82.7

Teng, F.-Z., Hu, Y., & Chauvel, C. (2016). Magnesium isotope geochemistry in arc volcanism. *Proceedings of the National Academy of Sciences*, *113*(26), 7082–7087. https://doi.org/10.1073/pnas.1518456113

Teng, F.-Z., Li, W.-Y., Ke, S., Marty, B., Dauphas, N., Huang, S., et al. (2010). Magnesium isotopic composition of the Earth and chondrites. *Geochimica et Cosmochimica Acta*, *74*(14), 4150–4166. https://doi.org/10.1016/j.gca.2010.04.019

Teng, F.-Z., Li, W.-Y., Rudnick, R. L., & Gardner, L. R. (2010). Contrasting lithium and magnesium isotope fractionation during continental weathering. *Earth and Planetary Science Letters*, *300*(1), 63–71. https://doi.org/10.1016/j.epsl.2010.09.036

Tessier, A., Campbell, P. G., & Bisson, M. (1979). Sequential extraction procedure for the speciation of particulate trace metals. *Analytical Chemistry*, *51*(7), 844–851. https://doi.org/10.1021/ac50043a017

Tibbett, E. J., Scher, H. D., Warny, S., Tierney, J. E., Passchier, S., & Feakins, S. J. (2021). Late Eocene record of hydrology and temperature from Prydz Bay, East Antarctica. *Paleoceanography and Paleoclimatology*, *36*(4), e2020PA004204. https://doi.org/10.1029/2020pa004204

Tipper, E., Galy, A., Gaillardet, J., Bickle, M., Elderfield, H., & Carder, E. (2006). The magnesium isotope budget of the modern ocean: Constraints from riverine magnesium isotope ratios. *Earth and Planetary Science Letters*, *250*(1–2), 241–253. https://doi.org/10.1016/j.epsl.2006.07.037

Tipper, E. T. (2022). *Magnesium isotopes: Tracer for the global biogeochemical cycle of magnesium past and present or archive of alteration?* Cambridge University Press.

Tipper, E. T., Calmels, D., Gaillardet, J., Louvat, P., Capmas, F., & Dubacq, B. (2012). Positive correlation between Li and Mg isotope ratios in the river waters of the Mackenzie Basin challenges the interpretation of apparent isotopic fractionation during weathering. *Earth and Planetary Science Letters*, *333–334*, 35–45. https://doi.org/10.1016/j.epsl.2012.04.023

Tochilin, C. J., Reiners, P. W., Thomson, S. N., Gehrels, G. E., Hemming, S. R., & Pierce, E. L. (2012). Erosional history of the Prydz Bay sector of East Antarctica from detrital apatite and zircon geo-and thermochronology multidating. *Geochemistry, Geophysics, Geosystems*, *13*(11). https://doi.org/10.1029/2012gc004364

Van Breedam, J., Huybrechts, P., & Crucifix, M. (2022). Modelling evidence for late Eocene Antarctic glaciations. *Earth and Planetary Science Letters*, *586*, 117532. https://doi.org/10.1016/j.epsl.2022.117532

Vance, D., Teagle, D. A., & Foster, G. L. (2009). Variable Quaternary chemical weathering fluxes and imbalances in marine geochemical budgets. *Nature*, *458*(7237), 493–496. https://doi.org/10.1038/nature07828

Westerhold, T., Marwan, N., Drury, A. J., Liebrand, D., Agnini, C., Anagnostou, E., et al. (2020). An astronomically dated record of Earth's climate and its predictability over the last 66 million years. *Science*, *369*(6509), 1383–1387. https://doi.org/10.1126/science.aba6853

Wilson, D. J., Piotrowski, A. M., Galy, A., & Clegg, J. A. (2013). Reactivity of neodymium carriers in deep sea sediments: Implications for boundary exchange and paleoceanography. *Geochimica et Cosmochimica Acta*, *109*, 197–221. https://doi.org/10.1016/j.gca.2013.01.042

Wimpenny, J., Burton, K. W., James, R. H., Gannoun, A., Mokadem, F., & Gíslason, S. R. (2011). The behaviour of magnesium and its isotopes during glacial weathering in an ancient shield terrain in West Greenland. *Earth and Planetary Science Letters*, *304*(1), 260–269. https://doi.org/10.1016/j.epsl.2011.02.008

Wimpenny, J., Colla, C. A., Yin, Q.-Z., Rustad, J. R., & Casey, W. H. (2014). Investigating the behaviour of Mg isotopes during the formation of clay minerals. *Geochimica et Cosmochimica Acta*, *128*, 178–194. https://doi.org/10.1016/j.gca.2013.12.012

Wombacher, F., Eisenhauer, A., Böhm, F., Gussone, N., Regenberg, M., Dullo, W. C., & Rüggeberg, A. (2011). Magnesium stable isotope fractionation in marine biogenic calcite and aragonite. *Geochimica et Cosmochimica Acta*, *75*(19), 5797–5818. https://doi.org/10.1016/j.gca.2011.07.017

Yoshimura, T., Araoka, D., Tamenori, Y., Kuroda, J., Kawahata, H., & Ohkouchi, N. (2018). Lithium, magnesium and sulfur purification from seawater using an ion chromatograph with a fraction collector system for stable isotope measurements. *Journal of Chromatography A*, *1531*, 157–162. https://doi.org/10.1016/j.chroma.2017.11.052

Young, G. M., & Nesbitt, H. W. (1998). Processes controlling the distribution of Ti and Al in weathering profiles, siliciclastic sediments and sedimentary rocks. *Journal of Sedimentary Research*, *68*(3), 448–455. https://doi.org/10.2110/jsr.68.448

Zachos, J., Pagani, M., Sloan, L., Thomas, E., & Billups, K. (2001). Trends, rhythms, and aberrations in global climate 65 Ma to present. *Science*, *292*(5517), 686–693. https://doi.org/10.1126/science.1059412

Zachos, J. C., & Kump, L. R. (2005). Carbon cycle feedbacks and the initiation of Antarctic glaciation in the earliest Oligocene. *Global and Planetary Change*, *47*(1), 51–66. https://doi.org/10.1016/j.gloplacha.2005.01.001

Zachos, J. C., Opdyke, B. N., Quinn, T. M., Jones, C. E., & Halliday, A. N. (1999). Early Cenozoic glaciation, Antarctic weathering, and seawater 87Sr/86Sr: Is there a link? *Chemical Geology*, *161*(1–3), 165–180. https://doi.org/10.1016/s0009-2541(99)00085-6

Zhang, Y. G., Lacan, F., & Jeandel, C. (2008). Dissolved rare earth elements tracing lithogenic inputs over the Kerguelen Plateau (Southern Ocean). *Deep Sea Research Part II: Topical Studies in Oceanography*, *55*(5), 638–652. https://doi.org/10.1016/j.dsr2.2007.12.029

Zhang, Y. G., Pagani, M., Liu, Z., Bohaty, S. M., & DeConto, R. (2013). A 40-million-year history of atmospheric CO_2. *Philosophical Transactions: Mathematical, Physical and Engineering Sciences*, *371*(2001), 1–20. https://doi.org/10.1098/rsta.2013.0096